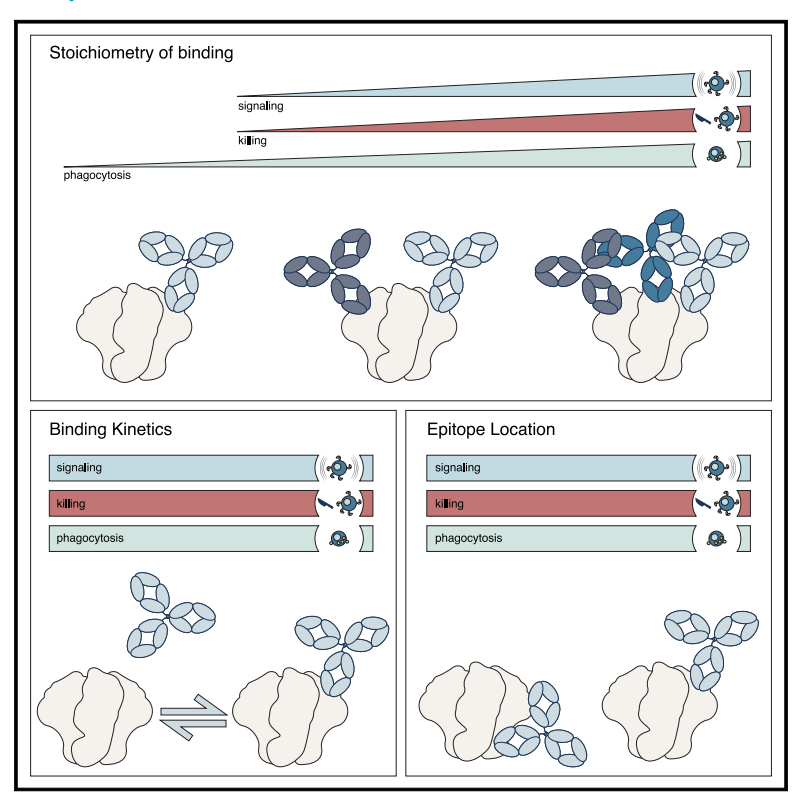
Molecular parameters governing antibody $Fc\gamma R$ signaling and effector functions in the context of HIV envelope

Graphical abstract



Authors

Michael V. Bick, Eduard Puig, David Beauparlant, ..., Andrew B. Ward, Dennis R. Burton, Lars Hangartner

Correspondence

Ihangart@scripps.edu

In brief

Bick et al. investigate the molecular factors influencing anti-HIV antibody Fc effector functions using Al-assisted protein design. They find that the stoichiometry of antibody binding is the primary determinant of $Fc\gamma RIIIa$ signaling and immune responses such as antibody-dependent cellular cytotoxicity and phagocytosis, while epitope location and binding kinetics have minimal impact.

Highlights

- Al structure prediction is used to generate epitope-grafted HIV envelope proteins
- Stoichiometry of binding is the key parameter for FcγRIIIa signaling and NK cell killing
- Bead acquisition by THP-1 cells or monocytes are less affected by stoichiometry
- Binding kinetics and epitope location have little impact on antibody effector functions







Article

Molecular parameters governing antibody Fc_γR signaling and effector functions in the context of HIV envelope

Michael V. Bick,^{1,7} Eduard Puig,^{1,7} David Beauparlant,^{1,7} Rebecca Nedellec,¹ Iszac Burton,¹ Keihvan Ardaghi,¹ Thea R. Zalunardo,¹ Raiza Bastidas,¹ Xuduo Li,¹ Javier Guenaga,^{1,2} Wen-Hsin Lee,³ Richard Wyatt,^{1,2} Wenwen Zhu,⁴ Max Crispin,^{4,5} Gabriel Ozorowski,^{3,5} Andrew B. Ward,^{2,3,5} Dennis R. Burton,^{1,2,5,6} and Lars Hangartner^{1,5,8,*}

SUMMARY

Antibody effector functions contribute to the immune response to pathogens and can influence the efficacy of antibodies as therapeutics. To date, however, there is limited information on the molecular parameters that govern fragment crystallizable (Fc) effector functions. In this study, using AI-assisted protein design, the influences of binding kinetics, epitope location, and stoichiometry of binding on cellular Fc effector functions were investigated using engineered HIV-1 envelope as a model antigen. For this antigen, stoichiometry of binding was found to be the primary molecular determinant of $Fc\gamma RIIIa$ signaling, antibody-dependent cellular cytotoxicity, and antibody-dependent cellular phagocytosis, while epitope location and antibody-binding kinetics, at least in the ranges investigated, were of no substantial impact. These findings are of importance for informing the development of vaccination strategies against HIV-1 and, possibly, other viral pathogens.

INTRODUCTION

The importance of fragment crystallizable (Fc) effector functions has been well studied for infectious diseases $^{1-17}$ and the treatment of malignancies 18 over a long time period. Fc effector functions are generally linked to antibody (cell surface) binding $^{19-22}$ and receptor crosslinking, 23,24 but detailed knowledge on the parameters that govern $Fc\gamma R$ signaling is sparse.

For instance, using artificial B cell tumor marker CD20 antigens, it was found that epitope proximity to the cellular membrane was favorable for antibody-dependent cellular cytotoxicity (ADCC) and complement-dependent cellular cytotoxicity (CDC), but membrane-distal binding abolished ADCC while facilitating antibody-dependent cellular phagocytosis (ADCP).²⁵ Furthermore, stoichiometry of binding has proven essential for anti-CD20 monoclonal antibodies (mAbs) to efficiently induce complement activation: complement-activating type I mAbs form seeding complexes that allow for the recruitment of additional antibodies to crosslink multiple CD20 dimers, while poor complement-activating type II mAbs form terminal 2:1 complexes that preclude the recruitment of additional antibodies and

CD20 molecules. 26 Additionally, antibody hexamer formation has been shown to enhance $Fc\gamma R$ engagement and complement activation. 27,28

For human immunodeficiency virus 1 (HIV-1), it was found that Fc effector functions but not complement were important for antibody-mediated protection for one 1,2 but not another broadly neutralizing antibody (bnAb). 4,29 Antiviral effector functions generally tend to correlate with viral neutralization, $^{19-22}$ albeit not in all cases. $^{20,30-33}$ For instance, Fc γ R engagement and triggering of ADCC have been shown to tolerate relatively poor antigen-binding kinetics as compared to neutralization, which was exemplified by the low avidity and high off-rate binding of HIV bnAb PGT145 to $SIV_{mac}239$ that was still able to trigger potent ADCC. 30

For influenza virus hemagglutinin (HA) stem-specific antibodies in mice, some degree of protection was lost if complement activation was abrogated, which was further exacerbated when Fc γ R binding was absent entirely. HA-stem-specific mAbs were shown to require interaction of the bound HA with its sialic acid (SA) receptor, in addition to the Fc/Fc γ R interactions, to trigger natural killer (NK) cell degranulation efficiently. By contrast, head-specific anti-HA antibodies were



¹Department of Immunology and Microbiology, The Scripps Research Institute, La Jolla, CA 92109, USA

²IAVI Neutralizing Antibody Center, The Scripps Research Institute, La Jolla, CA 92037, USA

³Department of Integrative Structural and Computational Biology, The Scripps Research Institute, La Jolla, CA 92109, USA

⁴School of Biological Sciences, University of Southampton, Southampton SO17 1BJ, UK

⁵Consortium for HIV/AIDS Vaccine Development (CHAVD), The Scripps Research Institute, La Jolla, CA 92037, USA

⁶Ragon Institute of Massachusetts General Hospital, Massachusetts Institute of Technology and Harvard University, Cambridge, MA 02139, USA

⁷These authors contributed equally

⁸Lead contact

^{*}Correspondence: lhangart@scripps.edu https://doi.org/10.1016/j.celrep.2025.115331



found to be generally poor inducers of ADCC³⁶ or neutrophil activation³⁷ and to inhibit stem antibody-mediated NK cell degranulation, presumably by interfering with HA/SA interactions.^{35,38} Multiple studies^{36–38} show that both head- and stem-specific antibodies can induce ADCP.³⁷

Despite these findings, there remains a significant knowledge gap as to what governs how effectively an antibody complexed to an antigen, particularly on an infected cell, will function. To this end, we developed a unique system that allows for the systematic examination of key molecular mechanisms of anti-HIV antibody-antigen interactions responsible for triggering Fc effector functions across epitopes of interest while avoiding common pitfalls related to variations in antibody composition. We generated an array of HIV-1 Envelope (Env) proteins engrafted with an HA tag at various key positions and used artificial intelligence (AI)informed design to express Env constructs in both membranebound and soluble forms. This system was then validated, and the constructs were used in conjunction with humanized anti-HA-tag mAb 12CA5 to characterize the role of antibody-binding avidity, epitope location, and stoichiometry in Fc₂R signaling, ADCC, and ADCP in the context of the HIV-1 Env protein.

RESULTS

Al-assisted generation of epitope-tagged membranebound and soluble HIV BG505-NFL proteins

In our initial studies using classical BG505- or JRFL-infected CEM.NKR-CCR5⁺Luc⁺ target cells (HIV reagent ARP-5198) and primary human NK cells, it was found that bnAbs whose epitopes were localized to V3 glycans mediated ADCC most effectively, followed by those binding the CD4bs. By contrast, V2/apex bnAbs were rather inefficient in triggering NK ADCC. However, ADCC assays using infected cells are afflicted by a high inter-assay and inter-donor variability, and results are further confounded by varying viral cytopathic effects and Env surface expression levels between viral isolates. Moreover, bnAbs can vary in their stoichiometry of binding, binding kinetics, and Fc glycosylation.

To overcome these limitations, Env constructs were developed, taking advantage of a highly stabilized BG505-NFL trimer, referred to as BG505-NFL.711, which was developed as a vaccine candidate for mRNA delivery.39 The HA tag (YPYDVPDYA),40 which is recognized by mAb 12CA5, a subclone of mAb H26D08, 41,42 was grafted onto different locations of the Env surface. The epitope grafts, referred to as roaming tags (RTs), were placed at distinct bnAb binding sites (V3, V2, CD4bs) or at sites commonly recognized by polyclonal antibodies following immunization with BG505 immunogens (V1, V4, C3V5, Bottom [Bttm]).43-47 Membrane-bound roaming tag constructs (mbRTs) were expressed on stably transfected HEK293T (293T) cell lines to be used as target cells, and soluble roaming tag proteins (sRTs) were produced for structural analysis and as targets for phagocytosis. For the mbRTs, the BG505-NFL.711 open reading frame was fused to a self-cleavable enhanced green fluorescent protein (GFP) gene to quantify Env expression levels.

AlphaFold2 *in silico* structure prediction (Figure 1),^{48,49} in conjunction with probabilistic residue interaction network anal-

ysis (Figure 1D), 50 indicated that the first iteration constructs recognized well by 12CA5, e.g., RT-V4, contained hydrogen bonds between epitope residues and a potentially glycosylated SNST or STNST motif downstream of the engrafted epitope. The importance of these downstream residues for 12CA5 binding was then confirmed by comparing mbRT-V1 designs (Figure 1E), and an SNST motif was added to the C terminus of the HA-tag sequence in most constructs (Figure 1B). For each construct, multiple in silico structure predictions were performed to assess microvariations in the respective graft designs, with the most promising design being selected for test expression. Successful epitope grafting with proper Env trimer folding was achieved for all constructs in the first or second design iteration, except for the CD4bs. The CD4bs proved challenging as a grafting site due to its recessed location and, according to in silico structure predictions, a strong propensity of the grafted epitope to fill void volumes within the trimer. Consequently, 12CA5 epitope recognition remained suboptimal in this construct (see below).

sRT-12CA5 fragment antigen binding (Fab) immune complexes were imaged by negative-stain electron microscopy (nsEM), and 3D reconstructions demonstrate 12CA5 binding to expected epitopes with some slight differences in angle of approach (Figures 1C and S1C). Grafted epitope flexibility can be appreciated in the RT-V4 and RT-Bttm constructs. The sRT-V2i construct tended to break up into protomers in solution and was not included in the nsEM analysis. Additionally, sRT-CD4bs exhibited poor binding avidity for 12CA5 and therefore could not be successfully imaged in complex. In addition, a full glycan analysis was performed, demonstrating glycosylation of added SNST sequons (Figure S2).

Basic characterization of epitope-grafted target cell lines

The stable 293T target cell lines varied in GFP and Env surface expression levels, as well as in percentage of GFP-positive cells (Figure S1A). For RT-V2i, two cell lines with divergent GFP and Env surface expression levels were generated to make a direct comparison of differing surface density for the same RT construct. Proper folding was confirmed by flow cytometry using PGT121 as a reference antibody in conjunction with PGT145, a mAb with high binding specificity for a closed Env trimer conformation, and non-native conformation-specific mAbs F105, 17b, and C11 (Figure S1B). RT-V2i failed to bind PGT145 or PGDM1400, as the tag is located within the V2/apex bnAb epitope, and V3-mediated shielding of the CD4bs was reduced, as evidenced by increased binding of F105. The tag in RT-V3 eradicated PGT121 binding and diminished PGT128 binding, while grafting of the 12CA5 epitope onto the V4 loop improved PGT145 binding. Overall, however, RT constructs were presented in a native closed conformation on the target cell lines.

Binding characteristics of bnAbs and 12CA5 to tagged Fnv

A set of binding experiments was conducted using mAb 12CA5, a panel of ten mAbs binding key epitopes of interest, and SARS-CoV-2-specific control mAb CC40.8.⁵¹ First, antibody cell-surface binding to mbRT constructs was assessed via flow

Article



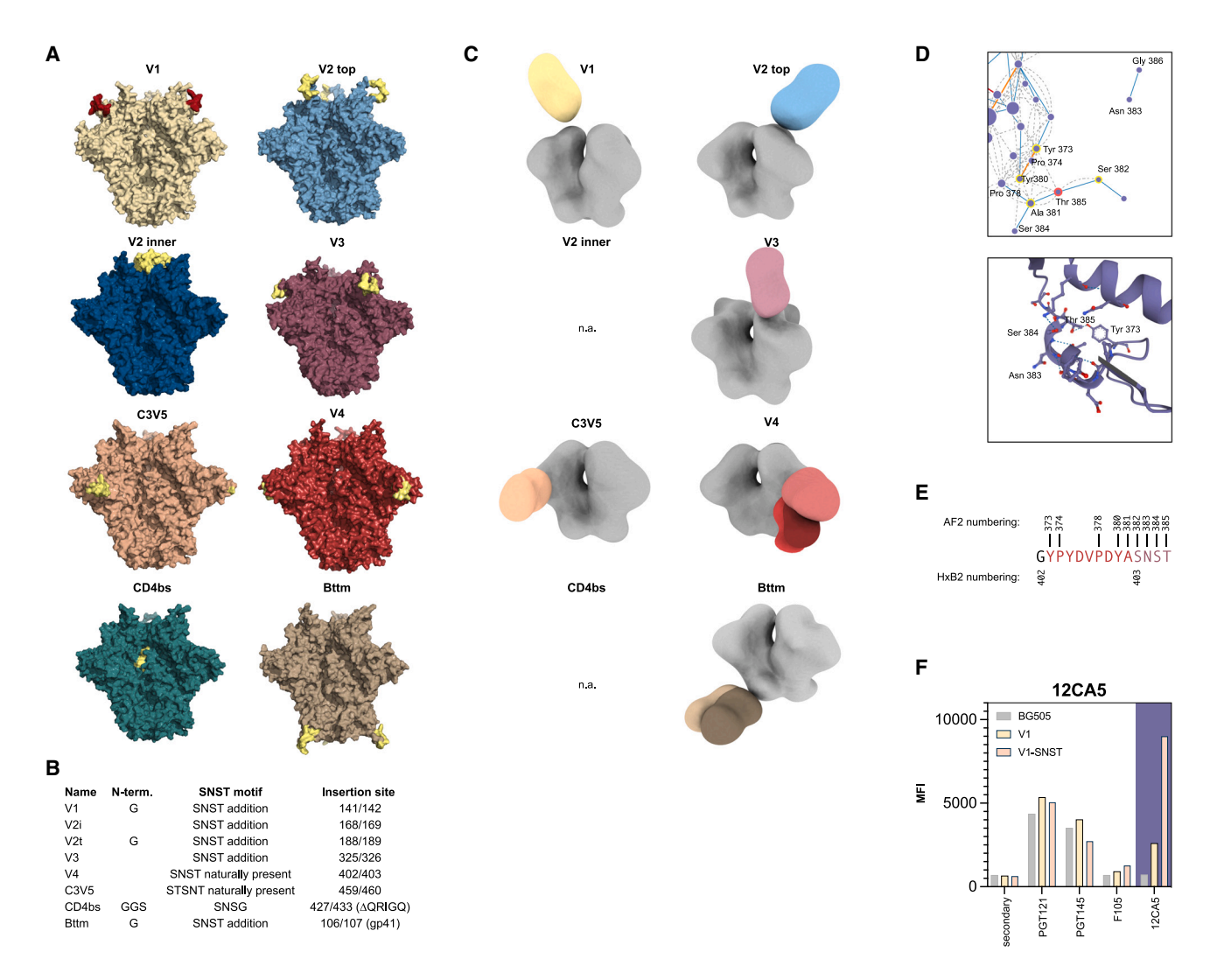


Figure 1. Overview of roaming tag constructs

- (A) AlphaFold2 structure predictions of the roaming tag constructs with the tag in yellow (red for V1).
- (B) Molecular details of the epitope grafting sites and tag modifications.
- (C) Negative-stain EM 3D reconstructions of 12CA5 Fab bound to the indicated roaming tag construct. Maps are segmented and colored by 12CA5 Fab and trimer (see also Figure S1C). Multiple 3D classes for RT-V4 and RT-Bttm indicate high epitope flexibility.
- (D) Probabilistic residue interaction network analysis⁵⁰ of the top 24 ranked AlphaFold2 structure predictions for RT-V4 identified several hydrogen bonds (solid lines) and van der Waals (dashed lines) interactions between the core epitope amino acids and the downstream SNST motif. Numbering refers to the AA position in the AlphaFold2 prediction.
- (E) Positions of the residues found to interact between the core epitope amino acids (red) and SNST motif (purple) in RT-V4. The AlphaFold2 residue numbers are displayed above the sequence and HxB2 numbering below.
- (F) Cell-surface binding comparison of RT-V1 recognition by 12CA5 with and without an added SNST motif using flow cytometry. Antibodies PGT121, PGT145, and F105 were added as conformation controls. Data shown represent results from one representative experiment of three.

cytometry. mbRT cell lines were incubated with titrated mAbs, and bound antibody was detected with an allophycocyanin (APC)-labeled secondary antibody (Figure 2). Cells were gated on GFP for mbRT construct expression, and the APC geometric mean fluorescence intensity (MFI) of GFP-positive cells was determined for each mAb concentration. Both membrane-bound mAb binding EC_{50} (mbEC₅₀) and maximal mAb binding were interpolated using a Hill-curve-based non-linear curve-fitting model (Figure 2A; GraphPad Prism 9 and 10). mbEC₅₀s

of bnAbs were similar across mbRT constructs, indicating similar access to the roaming tags aside from aforementioned antibody-epitope interactions disrupted by tag engraftment, whose data points were excluded from analysis. Of note, 12CA5 recognized RT-Bttm expressed as transmembrane protein, while the Bttm antibodies elicited by immunization typically only recognize soluble trimers.

In parallel, GFP MFI was averaged over all samples of a cell line (typically 192 individual data points). To confirm GFP



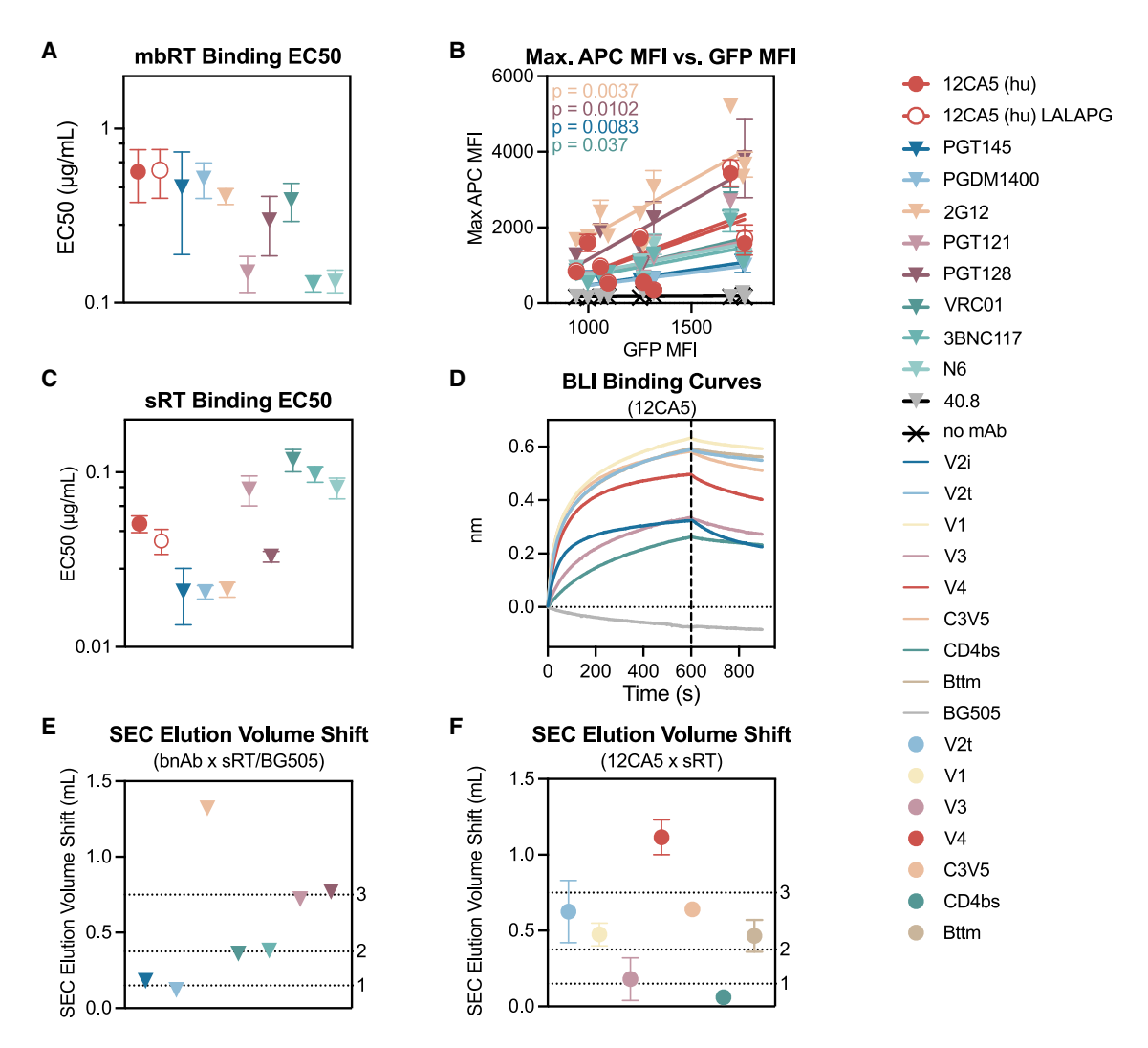


Figure 2. Biochemical characterization of RT constructs

(A) Half-maximal binding concentrations of 12CA5 and bnAbs for mbRT cell lines. Titrated 12CA5 (circles) and bnAbs (triangles) were incubated with all mbRT and control cell lines (i.e., mbRT-V1, V2t, V2i_Hi, V2i_Lo, V3, V4, C3V5, CD4bs, Bttm, and BG505) in two technical replicates before cells were washed and bound antibodies detected with a secondary antibody. Following flow cytometry, APC MFI was determined for GFP+ cells. Non-linear Hill-curve fitting was then used to determine membrane-bound EC₅₀ values. Data shown represent the mean and SEM for each antibody and all RT cell lines from 2–3 independent experiments. (B) Correlation between Env and GFP expression levels. Experimental data from (A) was used to determine the maximal antibody binding (interpolated top value of curve fit) and plotted against the GFP MFI averaged over 192 data points for each cell line. Averaged GFP MFI and maximal antibody binding (Max. APC MFI) were found to correlate significantly for most antibodies, as determined by simple linear correlation analysis (p < 0.05; 0.44 < $R^2 < 0.76$). Data shown represent the mean and SEM from 2–3 independent experiments.

(C) Half-maximal binding concentrations of 12CA5 and bnAbs for sRT proteins. Enzymatically biotinylated sRT and control proteins (i.e., sRT-V1, V2t, V3, V4, C3V5, CD4bs, Bttm, and BG505) were immobilized on neutravidin-coated (2 μ g/mL) ELISA plates. After washing, titrated amounts of 12CA5 (circles) and bnAbs (triangles) were incubated with sRTs in two technical replicates and detected by a peroxidase-labeled goat anti-human lgG, F(ab')₂-specific secondary antibody. After development, non-linear Hill-curve fitting was used to determine soluble EC₅₀ values. Data shown represent the mean and SEM for each antibody and all sRT constructs from two independent experiments.

(D) Binding kinetics of 12CA5 to sRT proteins. The same biotinylated sRT and control proteins were associated to and dissociated from Octet biosensors loaded with 12CA5. Data shown represent the mean from three independent experiments.

(E and F) Stoichiometry of binding of (E) bnAbs to sRT-BG505 and (F) 12CA5 to sRTs. Using SEC, the stoichiometry of binding was determined as described in Bianchi et al.⁴³ In brief, 50 μg of the indicated sRT protein were incubated overnight with or without 10-fold molar excess of the indicated antibody Fab. The respective elution volumes were determined for both the sRT alone and the immune complex. Elution volume shifts (mL) were calculated by subtracting the complex elution volume from the sRT elution volume. Data shown represent either the value for each bnAb with sRT-BG505 from one experiment or the mean and SEM for 12CA5 with each sRT from two independent experiments. Dashed lines indicate the probable stoichiometry of binding based on literature and historical data.

Article



fluorescence as an accurate metric for surface Env expression levels of each mbRT target cell line, correlation of maximal mAb binding (max. APC) with averaged GFP MFI was tested (Figure 2B). A statistically significant linear correlation ($\rho < 0.05$, Pearson two-tailed) between maximal mAb binding and GFP MFI was found for all but three antibodies. Hence, the averaged GFP MFI provides a suitable normalization factor to account for differing Env expression levels among the mbRT cell lines.

Binding characteristics of the same antibody panel to sRT constructs was assessed by ELISA (Figure 2C). EC_{50} values for the sRTs (sEC₅₀) were generally an order of magnitude lower than their mbRT counterparts. CD4bs-specific bnAbs 3BNC117 and N6, as well as V3-specific bnAb PGT121, demonstrated higher binding avidity for the mbRTs, while apex-specific bnAb PGT145 bound more strongly to the sRTs.

Similarly, in biolayer interferometry (BLI) measurements (Figures 2D and S3), binding kinetics of 12CA5 showed small variance across most constructs. On-rates were similar for six of the constructs, while sRT-V3 and sRT-CD4bs displayed relatively slower on-rates. Off-rates were comparable for five of the eight constructs, with sRT-V1, sRT-V2t, and sRT-Bttm having relatively slower off-rates. The result of these variances is a small range of avidities (K_D) across constructs.

Finally, the binding stoichiometries of the bnAb panel to BG505 and tag mAb 12CA5 with each sRT were assessed by size-exclusion chromatography (SEC) of trimers in complex with Fabs, as described in Bianchi et al. 43 In accordance with previous data, 43 V2-, CD4bs-, and V3-specific bnAbs bound with stoichiometries of 1, 2, and 3 Fab fragments per trimer, respectively (Figure 2E). By contrast, the SEC elution volume shift of trimer complexed with 2G12 was found to be considerably higher, perhaps in part due to the fact that 2G12 Fab fragments themselves eluted at around double the molecular weight of traditional Fab fragments, as one would expect of a domainexchanged antibody.⁵² When comparing SEC elution shift volumes of the sRT-12CA5 Fab complexes with those of the BG505-bnAb Fab complexes (Figure 2F), it was found that 12CA5 bound RT-V3 and RT-CD4bs with a stoichiometry of 1, while the remaining RTs bound with a stoichiometry of 2 or 3 (sRT-V2i was not analyzed, as mentioned previously). Notably, RT-V4 complexed with 12CA5 Fab had a larger SEC elution volume shift than the other RTs, which might be explained by the tag epitope's flexibility and location contributing to a disproportionately large apparent molecular weight.

Impact of binding parameters on FcYRIIIa signaling

To investigate how epitope location affected Fc γ RIlla signaling, an Fc γ RIlla-expressing Jurkat reporter cell line (Invivogen, jktl-nfat-cd16) was exposed to target cells preincubated with either 10 or 1 μ g/mL of antibody. In this reporter cell line, Fc γ RIlla signaling induces secretion of luciferase under the control of a nuclear factor of activated T cells (NFAT) promoter. Following overnight co-culture, secreted luciferase activity was measured and multiplied by a factor calculated by dividing the mean GFP MFI over all cell lines by the GFP MFI for the respective mbRT cell line to correct for differing Env expression levels. The percentage of GFP-positive cells for each cell line was not found

to substantially affect Fc γ RIIIa signaling, as Fc γ RIIIa signaling only decreased by 10% if the effector-to-target (E:T) ratio was halved (Figure S4).

A clear hierarchy of the epitope-binned normalized FcγRIIIa signal was found in that V3-binding bnAbs induced the strongest FcγRIIIa signals followed by CD4bs-binding bnAbs. In contrast, V2/apex-binding bnAbs did not induce FcγRIIIa signals above background levels (Figure 3A). Also, mAb 2G12 was found to induce significantly higher FcγRIIIa signals than any other bnAb or 12CA5. Statistical analysis of the epitope-binned expression-normalized FcγRIIIa signal strength revealed that most bnAb classes were significantly different from each other (one-way ANOVA). The signals induced by mAb 12CA5 bound to the various RT cell lines were found to be in the range of V3and CD4bs-specific bnAbs, except for RT-CD4bs whose poor binding of 12CA5 (Figures 2A and 2B) was also reflected in a very low FcγRIIIa signal. More importantly, however, there was no clear indication of a relationship between the epitope location and FcγRIIIa signaling strength: 12CA5 bound to cell lines tagged at V2/apex bnAb epitopes (V2i and V2t) and was able to trigger FcγRIIIa signaling, while the corresponding bnAbs did not (Figure 3C). Also, the signal strength of apically bound 12CA5 was similar to that of 12CA5 bound to RT-Bttm, and no obvious trend between epitope location and FcγRIIIa signal strength was apparent.

The expression-normalized Fc_YRIIIa signal strengths induced by saturating (10 μg/mL) and subsaturating (1 μg/mL) mAb concentrations were correlated with mbEC $_{50}$, normalized maximal mAb binding, and stoichiometry of binding (SEC shift; Figures 3B and 3C). While no significant correlation was found between Fc_YRIIIa signaling strength and mbEC₅₀ at either concentration, there were highly statistically significant correlations (Spearman's rho \sim 0.8, p < 0.0001) between Fc γ RIIIa signaling and both the maximal amount of antibody bound and the stoichiometry of binding (Figure 3C). Taken together, these data demonstrate that for HIV Env. the stoichiometry of binding, and hence, the maximal amount of antibody bound is the key determinant of FcγRIIIa signaling. In the HIV-1 model presented here, trimeric Env needs to be engaged by more than one antibody to trigger an FcγRIIIa signal. Binding avidity, by contrast, did not correlate with Fc_{\gamma}RIIIa signaling strength under the conditions

Molecular factors determining antibody-dependent cellular cytotoxicity

To address the impact of molecular binding parameters on ADCC mediated by primary natural killer (NK) cells, an assay that detects loss of GFP-positive cells following overnight incubation of primary NK cells with antibody-sensitized target cells was devised. As above, to compensate for differing Env expression levels, specific killing percentages were normalized by the relative GFP MFI (normalized % killing). Interestingly, a similar epitope hierarchy was found in that V3-specific bnAbs (including 2G12) mediated the best killing, followed by CD4bs-specific bnAbs (Figure 4A). In contrast, V2/apex-specific bnAbs PGT145 and PGDM1400 typically displayed less than 10% specific killing. Such a hierarchy was not observed for 12CA5-mediated killing of RT-expressing cell lines (Figure 4B). Target



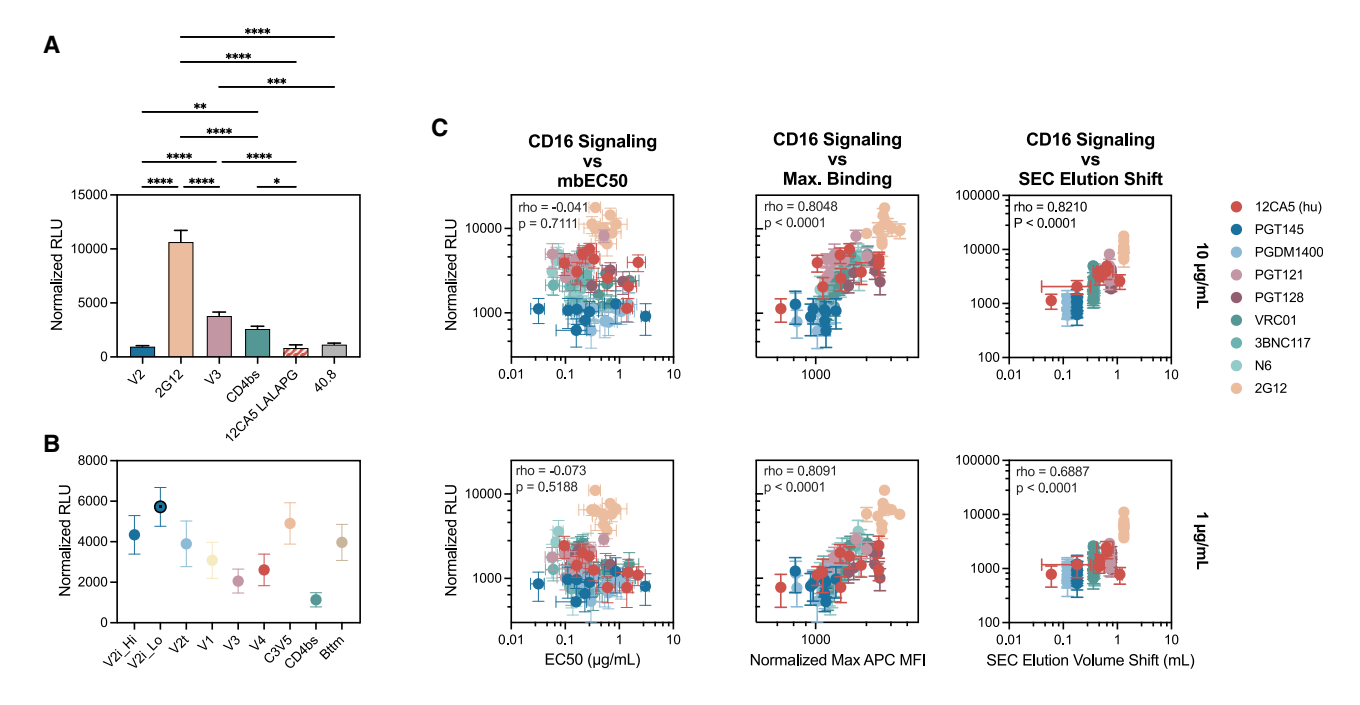


Figure 3. Molecular parameters governing FcγRIIIa signaling

Titrated amounts of the indicated antibody were allowed to bind to the RT cell lines before bound antibodies were detected by an APC-labeled anti-human antibody. Data from two technical replicates were then plotted against the antibody concentration, and both the mbEC $_{50}$ and max. APC values were determined by non-linear regression. In parallel, all mbRTs were incubated with a high (10 μ g/mL) and low (1 μ g/mL) concentration of the indicated endotoxin- and aggregate-free antibodies before Fc γ RIlla signaling-induced secretion of luciferase from Jurkat-CD16-NFAT-Luc reporter cells was determined following overnight co-culture at an effector-to-target ratio of 2:1. RLU and max. APC values were normalized against the pan-assay mean GFP MFI divided by the averaged GFP MFI for the respective cell line to correct for varying Env expression levels.

(A) Averaged normalized Fc γ RIIIa signal triggered by bnAbs at 10 μ g/mL. An epitope-dependent hierarchy for the Fc γ RIIIa signal strength (Normalized RLU) was found in that V3-specific bnAbs (PGT121, PGT128) induced the strongest signal, followed by antibodies binding to the CD4bs (VRC01, N6, 3BNC117). V2-specific bnAbs (PGDM1400, PGT145) failed to elicit Fc γ RIIIa signal above that of the negative control (40.8). By contrast, the signal induced by 2G12 was 2–4 times stronger than that induced by other bnAbs. Significant differences, as determined by one-way ANOVA tests, are indicated (*p < 0.05, **p < 0.001, ****p < 0.001, bata shown represent the mean and SEM of epitope-binned mAbs with all mbRTs from 2–3 experiment repetitions.

(B) Normalized signal triggered by 12CA5 at 10 μ g/mL. 12CA5 bound to various cell lines induced Fc γ RIIIa signal in the range of V3-specific bnAbs, except for 12CA5 bound to RT-V1, V3, and V4 inducing signals similar to CD4bs-specific bnAbs. Of note, 12CA5 bound to RT-V2i and V2t, located at the apex of the trimer, triggered Fc γ RIIIa signaling, while bnAbs binding to the same location did not. Data shown represent the mean and SEM of 12CA5 with each mbRT from 2–3 experiment repetitions.

(C) Impact of binding avidity, maximal amount of antibody bound, and stoichiometry of binding on Fc γ RIlla signal strength. Fc γ RIlla signal strength was determined for bnAbs and 12CA5 bound to both wild-type and RT target cell lines at saturating (10 μ g/mL) and subsaturating (1 μ g/mL) conditions and correlated with mbEC $_{50}$, normalized maximal antibody bound in flow cytometry (Max. binding), or stoichiometry of binding (SEC elution shift). Spearman's rho and two-tailed significance values are indicated. Data shown represent the mean and SEM from 2–3 experiment repetitions.

cells with an apically grafted epitope (V2i and V2t) were killed as efficiently as wild-type-expressing cells bound to V3/high-mannose patch (HMP)-specific bnAbs. Most efficient killing in the presence of 12CA5 was observed for V2t-tagged Env, followed by V4-, C3V5-, and V1-tagged Env. By contrast, target cells expressing V3-, CD4bs-, or Bttm-tagged Envs were not particularly efficiently killed.

Correlation analyses were performed to assess the impact of mbEC₅₀, normalized maximal mAb binding, and stoichiometry of binding on specific killing (Figure 4C). In line with analyses for Fc γ RIlla signaling, highly significant correlations (Spearman's rho \sim 0.75–0.8, p < 0.0001) were found for normalized maximal antibody bound and SEC elution shift but not binding kinetics (i.e., mbEC₅₀). Likewise, normalized killing and normalized Fc γ RIlla signaling significantly correlated (Spearman's rho \sim 0.7–0.76, p < 0.0001; Figure 4D). Despite these correlations,

there was an apparent plateau in killing at the highest Fc γ RIIIa signaling values induced by 2G12 at 10 μ g/mL (Figure 4D). Moreover, a discrepancy between Fc γ RIIIa signaling and killing was observed for mbRT-Bttm in that barely any killing was observed for this epitope location despite induction of a decent Fc γ RIIIa signal.



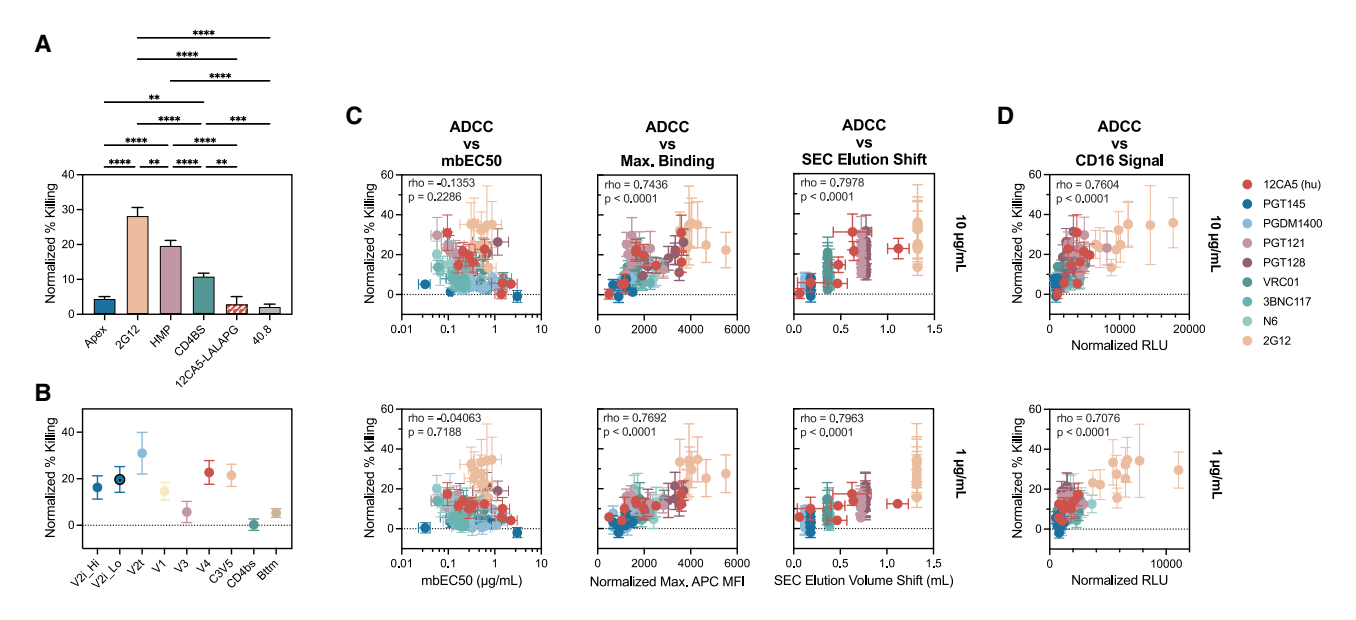


Figure 4. Molecular patterns governing ADCC by primary human NK cells

To determine antibody-mediated killing by primary NK cells (of 158V/V and 158V/F genotypes), an assay was developed that measured elimination of GFP⁺ wild-type Env- or RT Env-expressing cells following co-culture with primary human NK cells in the presence of either 10 or 1 µg/mL of endotoxin- and aggregate-free antibody in duplicate at an effector-to-target cell ratio of 5:1. The number of GFP⁺ cells in each co-culture was determined the next day, and specific killing was calculated by normalizing against the non-specific killing (number of GFP⁺ cells in co-cultures without antibody). 100% killing was defined as the complete absence of GFP-positive cells. To normalize for differing Env expression levels, values for specific killing were multiplied by a factor calculated by the pan-assay mean GFP MFI divided by the averaged GFP MFI for the respective cell line.

(A) Averaged normalized killing mediated by bnAbs at 10 μ g/mL. As for normalized Fc γ RIIIa signaling, an epitope-dependent hierarchy for normalized killing (normalized % killing) was found in that V3-specific bnAbs (PGT121, PGT128) induced the most potent killing, followed by antibodies binding the CD4bs (VRC01, N6, 3BNC117). While V2-specific bnAbs (PGDM1400, PGT145) failed to elicit Fc γ RIIIa signals significantly above that of the negative control (40.8), some marginal killing was observed. In contrast, 2G12 killing was similar to that observed for other V3-specific bnAbs. Significant differences, as determined by one-way ANOVA tests, are indicated (*p < 0.05, **p < 0.01, ***p < 0.001, ***p < 0.0001). Data shown represent the mean and SEM of epitope-binned mAbs with all mbRTs from a total of 4–6 experiment repetitions using NK cells from two donors.

(B) Normalized killing mediated by 12CA5 at 10 μg/mL. Data shown represent the mean and SEM of 12CA5 with each mbRT from a total of 4–6 experiment repetitions using NK cells from two donors.

(C) Impact of binding avidity, maximal amount of antibody bound, and stoichiometry of binding on ADCC. Normalized killing was determined for bnAbs or 12CA5 bound to both wild-type and RT target cell lines at saturating (10 µg/mL) and subsaturating (1 µg/mL) conditions and correlated with mbEC₅₀, normalized maximal antibody bound (Max. binding), or stoichiometry of binding (SEC elution shift). Spearman's rho and two-tailed significance values are indicated. Data shown represent the mean and SEM from a total of 4–6 experiment repetitions using NK cells from two donors.

(D) Correlation between normalized killing and $Fc_{\gamma}RIIIa$ signaling. Normalized killing data from (C) was correlated with normalized signaling data from Figure 3 and plotted against each other. Statistically significant correlations were found for both mAb concentrations, albeit plateauing of specific killing was observed for the high 2G12 concentration. Spearman's rho and two-tailed significance values are indicated.

Molecular factors determining antibody-dependent cellular phagocytosis

Employing the enzymatically C-terminally biotinylated sRTs, the THP-1 phagocytic score was determined for both bnAbs and 12CA5 (Figure 5). sRT-V2i was omitted for this analysis, due to its propensity to disintegrate into protomers in solution. In brief, neutravidin-coated fluorescein isothiocyanate (FITC)-labeled beads were saturated with biotinylated sRTs, washed, and incubated with titrated amounts of antibody. Following overnight incubation with THP-1 cells, the phagocytic score (FITC MFI \cdot %FITC+ cells) was determined by flow cytometry. Scores were corrected for background, and both maximal phagocytic score and half-maximal phagocytic score concentration (pEC50) values were derived analogously to maximal binding and mbEC50/sEC50 values using the Hill-curve-based non-linear curve fitting model.

Overall, a similar epitope hierarchy was observed as for FcγRIIIa signaling and ADCC, with the exception that V2/apexspecific bnAbs opsonized beads as well as CD4bs-specific bnAbs. In general, differences between bnAbs and the individual sRTs were not as drastic compared to other assays (Figure 5A). No statistically significant correlation could be found between sEC_{50} and pEC_{50} (Figure 5C) or between sEC_{50} and maximal phagocytic score (Figure 5D), albeit a distinct clustering was discernible for the latter: mAbs 2G12, PGT128, and 12CA5 displayed intermediate avidity yet performed better than the higher-avidity V2/apex or lower-avidity CD4bs bnAbs. While no significant correlations could be found among sEC_{50} and maximal phagocytic score, differences in maximal phagocytic score across bnAb epitopes could be explained by antibody stoichiometry as measured by SEC elution shift (Spearman's rho \sim 0.7, p < 0.0001; Figure 5E). Although this assay does not



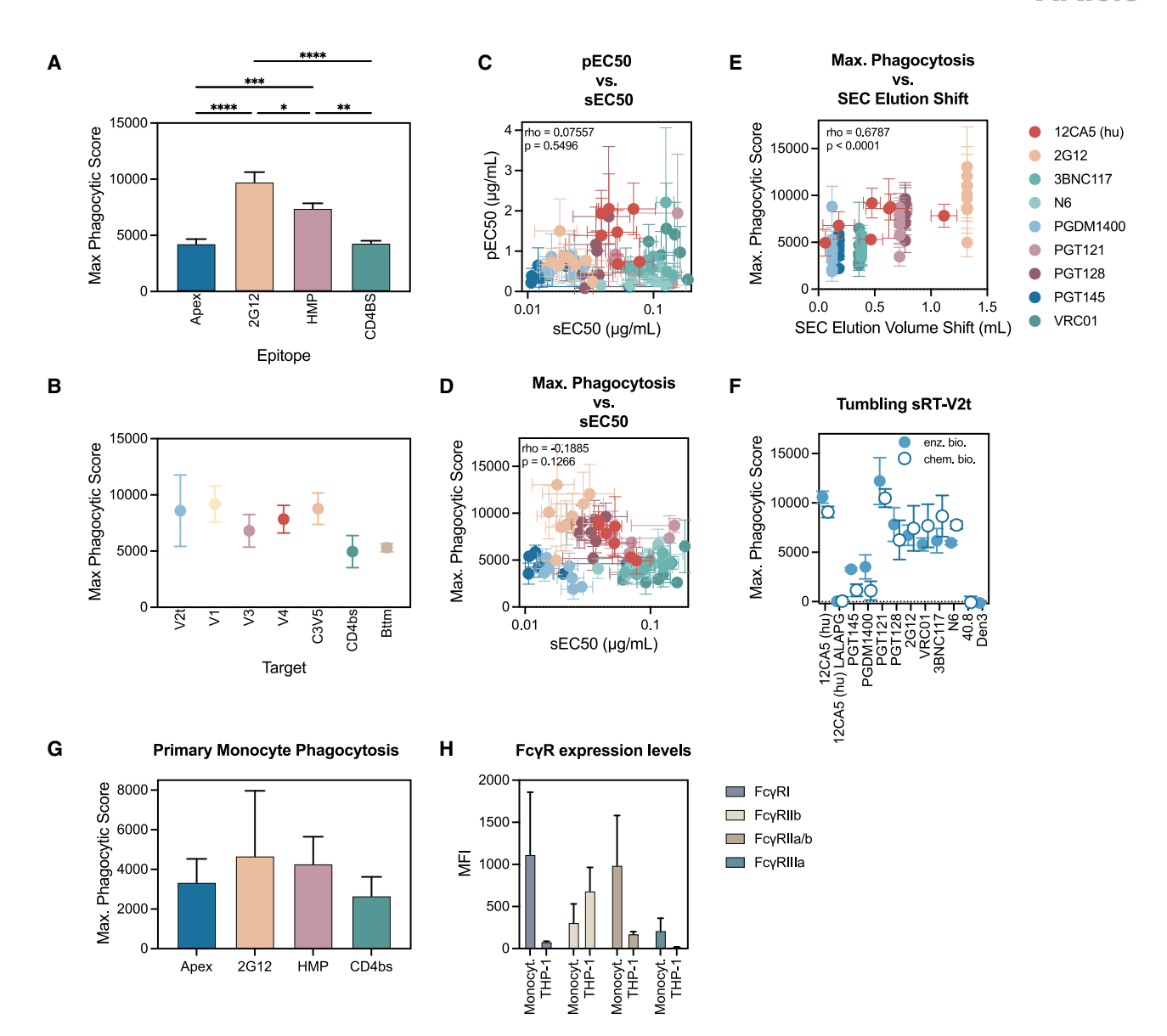


Figure 5. THP-1 phagocytosis of opsonized beads

One-micrometer-diameter neutravidin-coated FITC-labeled beads were saturated with biotinylated sRTs, washed, and incubated with titrated amounts of endotoxin- and aggregate-free antibody. After overnight incubation, bead acquisition was determined by flow cytometry. The phagocytic scores (FITC MFI \cdot % FITC+ cells) were background-corrected by subtraction of the phagocytic score for the negative controls. As above, non-linear curve fitting was used to determine both the mAb concentration conferring half-maximal phagocytosis (pEC₅₀) and the maximal phagocytic score.

(A) Epitope-binned maximal phagocytic score mediated by bnAbs at 10 μ g/mL. CD4bs (VRC01, 3BNC117, N6) and V2/apex-specific bnAbs (PGT145, PGDM1400) induced similar maximal phagocytic scores that were significantly lower than those for V3 (PGT121, PGT128) and 2G12, as determined by one-way ANOVA tests (*p < 0.05, **p < 0.01, ****p < 0.001, ****p < 0.0001). While the overall picture was similar to Fc γ RIlla signaling and killing, differences between epitopes were less prominent. No discernible phagocytosis above background was observed for beads opsonized using control antibodies Den3, 40.8, or 12CA5-LA-LAPG. Data shown represent the mean and SEM of epitope-binned mAbs with all sRTs from 2–3 experiment repetitions.

- (B) Maximal phagocytic score mediated by 12CA5 at 10 μg/mL. As above but with 12CA5 bound to the indicated sRT. Data shown represent the mean and SEM from 2–3 experiment repetitions.
- (C) Correlation between half-maximal phagocytic score (pEC₅₀) and sEC₅₀. No significant correlation was found between the half-maximal binding concentration, as determined by ELISA, and the half-maximal phagocytic concentration. Data shown represent the mean and SEM from 2–3 experiment repetitions.
- (D) Correlation between maximal phagocytic score and sEC_{50} . No significant correlation was found between the half-maximal binding concentration, as determined by ELISA, and the maximal phagocytic score. Data shown represent the mean and SEM from 2–3 experiment repetitions.
- (E) Correlation between maximal phagocytic score and stoichiometry of binding. A significant correlation was found between stoichiometry of binding (SEC elution shift) and the maximal phagocytic score.



differentiate between cell binding and uptake, these data suggest that efficacy of opsonized bead acquisition by THP-1 cells is less susceptible to molecular binding parameters than ADCC, but also largely correlates with the amount of antibody bound to the opsonized antigen, which is primarily dependent on the stoichiometry of binding.

To verify that epitope location has no impact on ADCP, both enzymatically (C-terminally) biotinylated and biochemically biotinylated RT-V2t were used to coat fluorescent beads. While the enzymatically biotinylated protein should adopt an orientation similar to that on virions, the orientation of the biochemically biotinylated RT-V2t should be random. As depicted in Figure 5F, only slight differences with no discernible trends were found in phagocytosis between the oriented and non-oriented antigen, again confirming that the epitope location, and likely the angle of approach, do not play a major role for phagocytosis.

Lastly, the ADCP experiments were repeated using primary monocytes instead of THP-1 cells as phagocytes (Figure 5G). A similar overall epitope hierarchy was found, albeit with apex-specific antibodies opsonizing more efficiently compared to THP-1 cells. The first difference is consistent with better apex mAb binding to RTv4 compared to wild-type Env. Our data indicate that the differing $Fc\gamma R$ expression pattern (Figure 5H), like the presence of $Fc\gamma Rl$ on monocytes, did not fundamentally affect the overall results.

In summary, the data presented demonstrate that stoichiometry of binding most strongly contributes to maximal phagocytic score, suggesting that Fc/Fc γ R interactions on phagocytes are governed by molecular mechanisms similar to that of Fc γ RIIIa on NK cells. Similarly, no influence from epitope location could be detected.

$\text{Fc}\gamma\text{RIIIa}$ signaling and ADCP mediated by antibody combinations

To further confirm the importance of the stoichiometry of binding for Fc γ RIIIa signaling and ADCP, assays were conducted with antibody combinations. As depicted in Figure S5, there was an additive effect on both Fc γ RIIIa signaling and ADCP for some but not all mAb combinations tested. Except for PGDM1400, all combinations of 12CA5 with apex or CD4bs bnAbs resulted in significantly stronger Fc γ RIIIa signaling than the individual antibodies. Also, there was a trend in that V2/apex bnAbs (stoichiometry of 1) combined with the majority of CD4bs (stoichiometry of 2) were more potent than the respective antibodies alone. This contrasted with combinations with HMP bnAb PGT128 (stoichiometry of 3), where little improvement over the PGT128 antibody was observed in combinations. Similar observations were made for ADCP, where combinations resulting in stoichiometries of greater than 3 were no more effective than those resulting in 3

(i.e., V2/apex plus CD4bs bnAbs). This indicates that either antibody binding or $Fc\gamma R$ interactions become somewhat restricted when more than three full-length immunoglobulin G1 (IgG1) molecules are bound per trimer.

DISCUSSION

For a variety of viral diseases-including influenza A, SARS-CoV-2, Chikungunya, Zika, Dengue, and Ebola-Fc effector functions have been shown to either enhance antibody-mediated protection or mitigate pathogenicity, 53,54 but this is not universally true across all mAbs. Similarly, for HIV, the role of Fc effector functions in immunity is complex. For example, the CD4bs-specific bnAb b12 showed a loss of approximately 50% of its protective efficacy when Fc-FcγR interactions were disrupted, whereas the V3-binding bnAb PGT121 did not exhibit significant Fc effector function contribution to protection.^{4,29} Additionally, non-neutralizing antibodies and effector function breadth^{55,56} have been associated with improved protection, ^{57–59} enhanced development of bnAbs, ⁶⁰ and lower viral loads in some cases. 61-63 However, passive immunization of non-human primates (NHPs) with non-neutralizing antibodies did not confer protection, 64,65 and initial associations between Fc-mediated protection in the RV144 vaccine trial⁵⁸ could not be replicated in the subsequent HVTN 702 study. 66

There is a surprising paucity of experimental data exploring the molecular parameters governing Fc effector functions. Previous assays designed to assess ADCC in HIV-infected cells have been fraught with artifacts 67-69 and strain-dependent cytopathic effects, variability in CD4 downregulation, and differences in viral replication and Env expression.^{68,70,71} To address these challenges, we utilized Al-guided in silico protein structure prediction, paired with recently developed stabilized Env trimers, to isolate the contributions of individual molecular parameters to Fc effector functions. By grafting single antibody epitopes onto distinct locations, we were able to eliminate confounding factors such as variations in Fc glycosylation. Additionally, coupling Env expression to GFP allowed for the normalization of results based on differences in surface expression levels, mitigating the issue of varying Env expression levels. This approach also facilitates high-throughput screening of serum samples from clinical trials, providing a more efficient system for evaluating Fc effector function. Al-based structure prediction, combined with meta-analysis using probabilistic residue network analysis, 50 significantly accelerated the development of this system. This approach enabled the generation of both membrane-bound and soluble Env designs with minimal experimental iterations. Meta-analysis of AlphaFold output proved helpful in prioritizing antigen designs, reducing the need for high-throughput experiments.

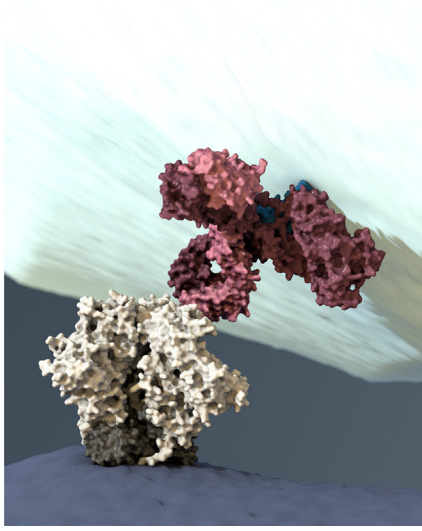
⁽F) Comparison of THP-1 phagocytosis between beads coated with enzymatically or biochemically biotinylated sRT-V2t. Beads were saturated with the indicated antigen and opsonized with titrated amounts of the indicated antibodies in duplicate. No discernible patterns were found between the enzymatically and biochemically biotinylated antigen. Data shown represent the mean and SEM for three experiment repetitions.

⁽G) Maximal phagocytic score for sRT-V4 and primary monocytes. As above but using human primary blood monocytes as effector cells. Data represent pooled and epitope-binned measurements from four independent experiments using three different donors. While similar trends can be observed with monocytes as for THP-1, differences did not achieve significance by one-way ANOVA, partially due to increased noise in the monocyte assay.

⁽H) $Fc\gamma R$ surface expression of THP-1 cells and primary monocytes determined by flow cytometry. Depicted are the averaged MFI values \pm SD for the indicated anti- $Fc\gamma R$ antibody from two independent experiments. Primary monocytes were isolated from two of the donors used in (G).







For HIV Env, data presented here demonstrate that stoichiometry of binding is the key determinant for two cellular effector functions, as it governs the maximal amount of antibody that can be bound and, hence, $Fc\gamma R$ signal strength. Moreover, it shows that antibodies binding with a stoichiometry of 1 are inefficient mediators of $Fc\gamma R$ effector functions, which parallels the observation that the complement non-activating anti-CD20 therapeutic obinutuzumab binds with a stoichiometry of 1, while the complement-activating rituximab was shown to bind CD20 with a stoichiometry of 2. 26,72 Conversely, when combining mAbs, the increase in $Fc\gamma R$ signaling was found to be the highest when the combined stoichiometry of binding was 3 or less (Figure S5B). Preliminary data suggest that trimers cannot accommodate binding of more than three full-length IgG molecules.

In cell-based assays, multiple Env trimers with bound antibodies are capable of clustering in proximity to each other, as transmembrane proteins generally exhibit lateral mobility on the cell membrane. In bead-based assays, we calculated that the theoretical minimum distance between trimers on fully saturated beads is approximately 2-2.5 nm, which is smaller than the trimer's diameter, enabling multiple Fc regions to be presented together. However, despite this proximity, bnAbs with a binding stoichiometry of 1 were still inefficient at triggering FcγR signals, highlighting that clustering Fc_YRs alone may not be sufficient for triggering effector functions. This finding also aligns with prior studies showing that FcYR signaling requires a minimum valency of 2 or more, with optimal activation often occurring at valencies of 5 or more.²⁴ Additionally, studies involving engineered IgG1 hexamers have demonstrated that the organization of Fc presentations can enhance complement activation and ADCC, reinforcing the importance of geometric considerations in Fcmediated immune responses. 27,73,74

Unexpectedly, the location and angle of antibody binding were found to have minimal impact on $Fc\gamma R$ engagement in our system. This contrasts with computational models of $Fc-Fc\gamma R$ interactions (Figure 6), which suggest that the antibody must adopt a bent conformation to properly engage membrane-bound $Fc\gamma Rs$.

Figure 6. Molecular model of FcγRlla (PDB: 3RY6) bound to PGT122 complexed with BG505 (PDB: 6B0N)

For the generation of the model, the Fc in the full-length $\lg G1$ structure of b12 (PDB: 1HZH) was aligned with the Fc in the $\digamma Fc\gamma Rlla/Fc$ structure before both were aligned via one Fab with the PGT122 Fab of PDB: 6B0N in PyMol. Surface meshes were then exported to Blender 3.6 and armature rigged, and Fab arms were moved to remove clashes between the Fab and $\digamma Fc\gamma Rlla$. The armature rigging was chosen, as the hinge region in the b12 structure PDB: 1HZH is poorly/partially resolved. Final figure composition and rendering was performed in Cinema4D.

In previous studies on the anti-CD20 mAb rituximab, epitope proximity to the membrane was found to influence ADCC, with membrane-distal epitopes being less effective at triggering effector functions.

However, in our study, the lack of significant impact from epitope location may be explained by the relatively short distance (9–10 nm) between the HIV Env apex and the membrane, a distance that was shown not to impede effector function.²⁵

Our data also indicate that primary NK cell killing of Env-expressing cells largely correlates with Fc γ RIIIa signal intensity, although the relationship plateaus at high signal strength. This suggests that NFAT-reporter cell lines, commonly used to assess ADCC, may overestimate the actual ADCC response under certain conditions. Notably, bnAb 2G12, a unique antibody with domain-exchanged Fab conformation, 52 displayed exceptional Fc effector function due to its exceptionally high stoichiometry of binding. 52 The unusually high Fc effector function of 2G12 may contribute to its remarkable protective efficacy in NHPs, 75 although further studies are needed to confirm this hypothesis.

Since neutralizing antibody concentrations required for full viral protection often exceed *in vitro* IC $_{50}$ values by several hundredfold, $^{76-80}$ vaccine strategies designed to induce bnAbs would benefit from Fc effector functions. Our findings suggest that off-target immune responses, such as those targeting V1, C3V5, and V4 epitopes, can also mediate Fc functions comparable to bnAbs. However, responses targeting the bottom epitope, present only on soluble proteins, would likely be ineffective. In NHP studies, protection correlated with autologous neutralizing titers, 81 but a diverse polyclonal antibody response, as seen in EM-based mapping, also seemed to contribute to protection. 44 These results suggest that Fc effector functions, especially those targeting V1, C3V5, and V4 epitopes, could possibly contribute to HIV vaccine efficacy.

Limitations of the study

As with most *in vitro* studies, the results here may not directly translate into correlates of protection. Additionally, each *in vivo* assay has specific limitations, as noted in the literature. While this study focused on key parameters of Fc-mediated immune responses, other factors, such as Fc organization and crosslinking, are also under investigation. Although HIV Env was the model

Article



antigen, our findings may be specific to this context, and other pathogens may have evolved different mechanisms to modulate antibody effector functions. Despite these limitations, this study offers valuable insights into the molecular parameters governing Fc effector functions, which will guide the design and evaluation of HIV vaccines and, potentially, other infectious disease vaccines or immunotherapies targeting malignancies.

RESOURCE AVAILABILITY

Lead contact

Requests for further information and resources should be directed to and will be fulfilled by the lead contact, Lars Hangartner (lhangart@scripps.edu).

Materials availability

Cell lines, antibodies, and soluble proteins generated in this study will be made available on request, but require a material transfer agreement for academic entities, or a payment and a completed materials transfer agreement if there is potential for commercial application.

Data and code availability

- All data presented in this study will be made available upon request. No code other than shell prompts to launch software mentioned in STAR Methods has been developed for this study. AF2 and AF3 containers have been modified/regenerated to avoid the use of the Anaconda repositories (AF2) and to match the installation requirements of our computer node. Although they are of limited use to other entities and subject to intellectual property owned by Google/Deepmind, the corresponding Dockerfiles will be made available on request.
- Representative electron density maps have been deposited in the Electron Microscopy DataBank under accession codes EMD-42907, EMD-42908, EMD-42909, EMD-42910, EMD-42912, and EMD-42913.

ACKNOWLEDGMENTS

This work was supported by the National Institutes of Health grants UM1 Al144462 (L.H., D.R.B., M.C., and A.B.W.) and R01 Al136621-05 (L.H. and A.B.W.), as well as European Molecular Biology Organization fellowship ALTF 339-2021 (E.P.), and Swiss National Science Foundation (SNSF) Fellowship P2ZHP3-174834 (D.B.).

AUTHOR CONTRIBUTIONS

This study was conceptualized by L.H., M.V.B., E.P., and D.R.B. L.H., E.P., and D.B. developed the RT constructs, with L.H. and E.P. performing Al structure predictions. Experimental methodologies were developed by M.V.B., R.N., E.P., and I.B. M.V.B., R.N., I.B., E.P., and D.B. performed most of the experimental work, with assistance from K.A., T.R.Z., and R.B. Experimental design, planning, and coordination were done by M.V.B. and R.N. X.L. assisted with cell sorting. J.G. and R.W. designed and kindly provided BG505-NFL.711. W.-H.L., G.O., and A.B.W. performed negative-stain electron microscopy W.Z. and M.C. provided glycoanalyses. Data analysis was performed by M.V.B. and L.H., who also wrote the manuscript. D.R.B. provided infrastructure, instrumentation, advice, and critical review of the manuscript. All authors reviewed the manuscript. L.H. supervised the study.

DECLARATION OF INTERESTS

The authors declare no competing interests.

STAR***METHODS**

Detailed methods are provided in the online version of this paper and include the following:

• KEY RESOURCES TABLE

- EXPERIMENTAL MODEL AND STUDY PARTICIPANT DETAILS
- METHOD DETAILS
 - Expression constructs
 - o Generation of stable HEK293T cell lines
 - o sRT production
 - Cell binding assay
 - FcγR FACS
 - FcγRIIIa signaling assays
 - ADCP assay
 - NK cell isolation
 - Monocyte isolation
 - o ADCC assay
 - o Binding ELISA
 - Biolayer interferometry
 - o Fab digestion
 - Complex formation
 - Negative-stain electron microscopy
 - Glycoanalysis
 - o PBMC isolation
- QUANTIFICATION AND STATISTICAL ANALYSES

SUPPLEMENTAL INFORMATION

Supplemental information can be found online at https://doi.org/10.1016/j.celrep.2025.115331.

Received: December 4, 2023 Revised: October 29, 2024 Accepted: January 28, 2025 Published: March 28, 2025

REFERENCES

- Hessell, A.J., Hangartner, L., Hunter, M., Havenith, C.E.G., Beurskens, F.J., Bakker, J.M., Lanigan, C.M.S., Landucci, G., Forthal, D.N., Parren, P.W.H.I., et al. (2007). Fc receptor but not complement binding is important in antibody protection against HIV. Nature 449, 101–104. https:// doi.org/10.1038/nature06106.
- Hessell, A.J., Poignard, P., Hunter, M., Hangartner, L., Tehrani, D.M., Bleeker, W.K., Parren, P.W.H.I., Marx, P.A., and Burton, D.R. (2009). Effective, low-titer antibody protection against low-dose repeated mucosal SHIV challenge in macaques. Nat. Med. 15, 951–954. https://doi.org/10.1038/nm.1974.
- Alter, G., Yu, W.H., Chandrashekar, A., Borducchi, E.N., Ghneim, K., Sharma, A., Nedellec, R., McKenney, K.R., Linde, C., Broge, T., et al. (2020). Passive Transfer of Vaccine-Elicited Antibodies Protects against SIV in Rhesus Macaques. Cell 183, 185–196. https://doi.org/10.1016/j. cell 2020 08 033
- Hangartner, L., Beauparlant, D., Rakasz, E., Nedellec, R., Hozé, N., McKenney, K., Martins, M.A., Seabright, G.E., Allen, J.D., Weiler, A.M., et al. (2021). Effector function does not contribute to protection from virus challenge by a highly potent HIV broadly neutralizing antibody in nonhuman primates. Sci. Transl. Med. 13, eabe3349. https://doi.org/10. 1126/scitranslmed.abe3349.
- Winkler, E.S., Gilchuk, P., Yu, J., Bailey, A.L., Chen, R.E., Chong, Z., Zost, S.J., Jang, H., Huang, Y., Allen, J.D., et al. (2021). Human neutralizing antibodies against SARS-CoV-2 require intact Fc effector functions for optimal therapeutic protection. Cell 184, 1804–1820. https://doi.org/10. 1016/j.cell.2021.02.026.
- Wang, P., Gajjar, M.R., Yu, J., Padte, N.N., Gettie, A., Blanchard, J.L., Russell-Lodrigue, K., Liao, L.E., Perelson, A.S., Huang, Y., and Ho, D.D. (2020).
 Quantifying the contribution of Fc-mediated effector functions to the antiviral activity of anti-HIV-1 IgG1 antibodies in vivo. Proc. Natl. Acad. Sci. USA 117, 18002–18009. https://doi.org/10.1073/pnas.2008190117.



- Zohar, T., and Alter, G. (2020). Dissecting antibody-mediated protection against SARS-CoV-2. Nat. Rev. Immunol. 20, 392–394. https://doi.org/ 10.1038/s41577-020-0359-5.
- Dias, A.G., Jr., Atyeo, C., Loos, C., Montoya, M., Roy, V., Bos, S., Narvekar, P., Singh, T., Katzelnick, L.C., Kuan, G., et al. (2022). Antibody Fc characteristics and effector functions correlate with protection from symptomatic dengue virus type 3 infection. Sci. Transl. Med. 14, eabm3151. https://doi.org/10.1126/scitranslmed.abm3151.
- Corti, D., Voss, J., Gamblin, S.J., Codoni, G., Macagno, A., Jarrossay, D., Vachieri, S.G., Pinna, D., Minola, A., Vanzetta, F., et al. (2011). A Neutralizing Antibody Selected from Plasma Cells That Binds to Group 1 and Group 2 Influenza A Hemagglutinins. Science 333, 850–856. https://doi. org/10.1126/science.1205669.
- Gunn, B.M., McNamara, R.P., Wood, L., Taylor, S., Devadhasan, A., Guo, W., Das, J., Nilsson, A., Shurtleff, A., Dubey, S., et al. (2023). Antibodies against the Ebola virus soluble glycoprotein are associated with longterm vaccine-mediated protection of non-human primates. Cell Rep. 42, 112402. https://doi.org/10.1016/j.celrep.2023.112402.
- Ilinykh, P.A., Huang, K., Santos, R.I., Gilchuk, P., Gunn, B.M., Karim, M.M., Liang, J., Fouch, M.E., Davidson, E., Parekh, D.V., et al. (2020). Nonneutralizing Antibodies from a Marburg Infection Survivor Mediate Protection by Fc-Effector Functions and by Enhancing Efficacy of Other Antibodies. Cell Host Microbe 27, 976–991. https://doi.org/10.1016/j.chom. 2020.03.025.
- Bootz, A., Karbach, A., Spindler, J., Kropff, B., Reuter, N., Sticht, H., Winkler, T.H., Britt, W.J., and Mach, M. (2017). Protective capacity of neutralizing and non-neutralizing antibodies against glycoprotein B of cytomegalovirus. PLoS Pathog. 13, e1006601. https://doi.org/10.1371/journal. ppat.1006601.
- Lefrancois, L., and Lyles, D.S. (1982). The interaction of antibody with the major surface glycoprotein of vesicular stomatitis virus. II. Monoclonal antibodies of nonneutralizing and cross-reactive epitopes of Indiana and New Jersey serotypes. Virology 121, 168–174. https://doi.org/10.1016/ 0042-6822(82)90126-x.
- Lefrancois, L. (1984). Protection Against Lethal Viral Infection by Neutralizing and Nonneutralizing Monoclonal Antibodies: Distinct Mechanisms of Action In Vivo. J. Virol. 51, 208–214. https://doi.org/10.1163/2210-7975 hrd-1326-0261.
- Schmaljohn, A.L., Johnson, E.D., Dalrymple, J.M., and Cole, G.A. (1982).
 Non-neutralizing monoclonal antibodies can prevent lethal alphavirus encephalitis. Nature 297, 70–72. https://doi.org/10.1038/297070a0.
- Henry Dunand, C.J., Leon, P.E., Huang, M., Choi, A., Chromikova, V., Ho, I.Y., Tan, G.S., Cruz, J., Hirsh, A., Zheng, N.-Y., et al. (2016). Both Neutralizing and Non-Neutralizing Human H7N9 Influenza Vaccine-Induced Monoclonal Antibodies Confer Protection. Cell Host Microbe 19, 800–813. https://doi.org/10.1016/j.chom.2016.05.014.
- Yamin, R., Jones, A.T., Hoffmann, H.-H., Schäfer, A., Kao, K.S., Francis, R.L., Sheahan, T.P., Baric, R.S., Rice, C.M., Ravetch, J.V., and Bournazos, S. (2021). Fc-engineered antibody therapeutics with improved anti-SARS-CoV-2 efficacy. Nature 599, 465–470. https://doi.org/10.1038/s41586-021-04017-w.
- Baldo, B.A. (2016). Monoclonal antibodies approved for cancer therapy. In Safety of Biologics Therapy: Monoclonal Antibodies, Cytokines, Fusion Proteins, Hormones, Enzymes, Coagulation Proteins, Vaccines, Botulinum Toxins (Springer), pp. 57–140. https://doi.org/10.1007/978-3-319-30472-4 3.
- Bruel, T., Guivel-Benhassine, F., Amraoui, S., Malbec, M., Richard, L., Bourdic, K., Donahue, D.A., Lorin, V., Casartelli, N., Noël, N., et al. (2016). Elimination of HIV-1-infected cells by broadly neutralizing anti-bodies. Nat. Commun. 7, 10844. https://doi.org/10.1038/ncomms10844.
- Bruel, T., Guivel-Benhassine, F., Lorin, V., Lortat-Jacob, H., Baleux, F., Bourdic, K., Noël, N., Lambotte, O., Mouquet, H., and Schwartz, O. (2017). Lack of ADCC Breadth of Human Nonneutralizing Anti-HIV-1 Anti-bodies. J. Virol. 91, e02440-16. https://doi.org/10.1128/jvi.02440-16.

- Spencer, D.A., Goldberg, B.S., Pandey, S., Ordonez, T., Dufloo, J., Barnette, P., Sutton, W.F., Henderson, H., Agnor, R., Gao, L., et al. (2022). Phagocytosis by an HIV antibody is associated with reduced viremia irrespective of enhanced complement lysis. Nat. Commun. 13, 662. https://doi.org/10.1038/s41467-022-28250-7.
- Ren, Y., Korom, M., Truong, R., Chan, D., Huang, S.-H., Kovacs, C.C., Benko, E., Safrit, J.T., Lee, J., Garbán, H., et al. (2018). Susceptibility to Neutralization by Broadly Neutralizing Antibodies Generally Correlates with Infected Cell Binding for a Panel of Clade B HIV Reactivated from Latent Reservoirs. J. Virol. 92, 008955. https://doi.org/10.1128/jvi. 00895-18.
- 23. Robinett, R.A., Guan, N., Lux, A., Biburger, M., Nimmerjahn, F., and Meyer, A.S. (2018). Dissecting $Fc\gamma R$ Regulation through a Multivalent Binding Model. Cell Syst. 7, 41–48. https://doi.org/10.1016/j.cels.2018. 05.018.
- Ortiz, D.F., Lansing, J.C., Rutitzky, L., Kurtagic, E., Prod'homme, T., Choudhury, A., Washburn, N., Bhatnagar, N., Beneduce, C., Holte, K., et al. (2016). Elucidating the interplay between IgG-Fc valency and FcγR activation for the design of immune complex inhibitors. Sci. Transl. Med. 8, 365ra158. https://doi.org/10.1126/scitranslmed.aaf9418.
- Cleary, K.L.S., Chan, H.T.C., James, S., Glennie, M.J., and Cragg, M.S. (2017). Antibody Distance from the Cell Membrane Regulates Antibody Effector Mechanisms. J. Immunol. 198, 3999–4011. https://doi.org/10. 4049/jimmunol.1601473.
- Kumar, A., Planchais, C., Fronzes, R., Mouquet, H., and Reyes, N. (2020).
 Binding mechanisms of therapeutic antibodies to human CD20. Science 369, 793–799. https://doi.org/10.1126/science.abb8008.
- 27. de Jong, R.N., Beurskens, F.J., Verploegen, S., Strumane, K., van Kampen, M.D., Voorhorst, M., Horstman, W., Engelberts, P.J., Oostindie, S.C., Wang, G., et al. (2016). A Novel Platform for the Potentiation of Therapeutic Antibodies Based on Antigen-Dependent Formation of IgG Hexamers at the Cell Surface. PLoS Biol. 14, e1002344. https://doi.org/10.1371/journal.pbio.1002344.
- Diebolder, C.A., Beurskens, F.J., de Jong, R.N., Koning, R.I., Strumane, K., Lindorfer, M.A., Voorhorst, M., Ugurlar, D., Rosati, S., Heck, A.J.R., et al. (2014). Complement is activated by IgG hexamers assembled at the cell surface. Science 343, 1260–1263. https://doi.org/10.1126/science.1248943.
- Parsons, M.S., Lee, W.S., Kristensen, A.B., Amarasena, T., Khoury, G., Wheatley, A.K., Reynaldi, A., Wines, B.D., Hogarth, P.M., Davenport, M.P., and Kent, S.J. (2019). Fc-dependent functions are redundant to efficacy of anti-HIV antibody PGT121 in macaques. J. Clin. Invest. 129, 182–191. https://doi.org/10.1172/jci122466.
- Bredow, B. von, Andrabi, R., Grunst, M., Grandea, A.G., Le, K., Song, G., Berndsen, Z.T., Porter, K., Pallesen, J., Ward, A.B., et al. (2019). Differences in the Binding Affinity of an HIV-1 V2 Apex-Specific Antibody for the SIVsmm/mac Envelope Glycoprotein Uncouple Antibody-Dependent Cellular Cytotoxicity from Neutralization. mBio 10, e01255-19. https://doi.org/10.1128/mbio.01255-19.
- von Bredow, B., Arias, J.F., Heyer, L.N., Moldt, B., Le, K., Robinson, J.E., Zolla-Pazner, S., Burton, D.R., and Evans, D.T. (2016). Comparison of Antibody-Dependent Cell-Mediated Cytotoxicity and Virus Neutralization by HIV-1 Env-Specific Monoclonal Antibodies. J. Virol. 90, 6127–6139. https://doi.org/10.1128/jvi.00347-16.
- Mayr, L.M., Decoville, T., Schmidt, S., Laumond, G., Klingler, J., Ducloy, C., Bahram, S., Zolla-Pazner, S., and Moog, C. (2017). Non-neutralizing Antibodies Targeting the V1V2 Domain of HIV Exhibit Strong Antibody-Dependent Cell-mediated Cytotoxic Activity. Sci. Rep. 7, 12655. https:// doi.org/10.1038/s41598-017-12883-6.
- Grunst, M.W., Ladd, R.A., Clark, N.M., Gil, H.M., Klenchin, V.A., Mason, R., Franchini, G., Roederer, M., and Evans, D.T. (2023). Antibody-dependent cellular cytotoxicity, infected cell binding and neutralization by antibodies to the SIV envelope glycoprotein. PLoS Pathog. 19, e1011407. https://doi.org/10.1371/journal.ppat.1011407.

Article



- Edgar, J.E., Trezise, S., Anthony, R.M., Krammer, F., Palese, P., Ravetch, J.V., and Bournazos, S. (2023). Antibodies elicited in humans upon chimeric hemagglutinin-based influenza virus vaccination confer FcγR-dependent protection in vivo. Proc. Natl. Acad. Sci. USA 120, e2314905120. https:// doi.org/10.1073/pnas.2314905120.
- Leon, P.E., He, W., Mullarkey, C.E., Bailey, M.J., Miller, M.S., Krammer, F., Palese, P., and Tan, G.S. (2016). Optimal activation of Fc-mediated effector functions by influenza virus hemagglutinin antibodies requires two points of contact. Proc. Natl. Acad. Sci. USA 113, E5944–E5951. https://doi.org/10.1073/pnas.1613225113.
- DiLillo, D.J., Tan, G.S., Palese, P., and Ravetch, J.V. (2014). Broadly neutralizing hemagglutinin stalk-specific antibodies require FcγR interactions for protection against influenza virus in vivo. Nat. Med. 20, 143–151. https://doi.org/10.1038/nm.3443.
- Mullarkey, C.E., Bailey, M.J., Golubeva, D.A., Tan, G.S., Nachbagauer, R., He, W., Novakowski, K.E., Bowdish, D.M., Miller, M.S., and Palese, P. (2016). Broadly Neutralizing Hemagglutinin Stalk-Specific Antibodies Induce Potent Phagocytosis of Immune Complexes by Neutrophils in an Fc-Dependent Manner. mBio 7, e01624-16. https://doi.org/10.1128/ mbio.01624-16.
- He, W., Tan, G.S., Mullarkey, C.E., Lee, A.J., Lam, M.M.W., Krammer, F., Henry, C., Wilson, P.C., Ashkar, A.A., Palese, P., and Miller, M.S. (2016). Epitope specificity plays a critical role in regulating antibody-dependent cell-mediated cytotoxicity against influenza A virus. Proc. Natl. Acad. Sci. USA 113, 11931–11936. https://doi.org/10.1073/pnas. 1609316113.
- Guenaga, J., Alirezaei, M., Feng, Y., Alameh, M.G., Lee, W.H., Baboo, S., Cluff, J., Wilson, R., Bale, S., Ozorowski, G., et al. (2024). mRNA lipid nanoparticles expressing cell-surface cleavage independent HIV Env trimers elicit autologous tier-2 neutralizing antibodies. Front Immunol. 15, 1426232. https://doi.org/10.3389/fimmu.2024.142623.
- Wilson, I.A., Niman, H.L., Houghten, R.A., Cherenson, A.R., Connolly, M.L., and Lerner, R.A. (1984). The structure of an antigenic determinant in a protein. Cell 37, 767–778.
- Niman, H.L., Houghten, R.A., Walker, L.E., Reisfeld, R.A., Wilson, I.A., Hogle, J.M., and Lerner, R.A. (1983). Generation of protein-reactive antibodies by short peptides is an event of high frequency: implications for the structural basis of immune recognition. Proc. Natl. Acad. Sci. USA 80, 4949–4953. https://doi.org/10.1073/pnas.80.16.4949.
- Field, J., Nikawa, J., Broek, D., MacDonald, B., Rodgers, L., Wilson, I.A., Lerner, R.A., and Wigler, M. (1988). Purification of a RAS-Responsive Adenylyl Cyclase Complex from Saccharomyces cerevisiae by Use of an Epitope Addition Method. Mol. Cell Biol. 8, 2159–2165. https://doi.org/ 10.1128/mcb.8.5.2159-2165.1988.
- Bianchi, M., Turner, H.L., Nogal, B., Cottrell, C.A., Oyen, D., Pauthner, M., Bastidas, R., Nedellec, R., McCoy, L.E., Wilson, I.A., et al. (2018). Electron-Microscopy-Based Epitope Mapping Defines Specificities of Polyclonal Antibodies Elicited during HIV-1 BG505 Envelope Trimer Immunization. Immunity 49, 288–300. https://doi.org/10.1016/j.immuni.2018.07.009.
- Nogal, B., Bianchi, M., Cottrell, C.A., Kirchdoerfer, R.N., Sewall, L.M., Turner, H.L., Zhao, F., Sok, D., Burton, D.R., Hangartner, L., and Ward, A.B. (2020). Mapping Polyclonal Antibody Responses in Non-human Primates Vaccinated with HIV Env Trimer Subunit Vaccines. Cell Rep. 30, 3755–3765. https://doi.org/10.1016/j.celrep.2020.02.061.
- Antanasijevic, A., Bowman, C.A., Kirchdoerfer, R.N., Cottrell, C.A., Ozorowski, G., Upadhyay, A.A., Cirelli, K.M., Carnathan, D.G., Enemuo, C.A., Sewall, L.M., et al. (2022). From structure to sequence: Antibody discovery using cryoEM. Sci. Adv. 8, eabk2039. https://doi.org/10.1126/sciadv.abk2039.
- Cirelli, K.M., Carnathan, D.G., Nogal, B., Martin, J.T., Rodriguez, O.L., Upadhyay, A.A., Enemuo, C.A., Gebru, E.H., Choe, Y., Viviano, F., et al. (2020). Slow Delivery Immunization Enhances HIV Neutralizing Antibody

- and Germinal Center Responses via Modulation of Immunodominance. Cell 180, 206. https://doi.org/10.1016/j.cell.2019.12.027.
- Dingens, A.S., Pratap, P., Malone, K., Hilton, S.K., Ketas, T., Cottrell, C.A., Overbaugh, J., Moore, J.P., Klasse, P.J., Ward, A.B., and Bloom, J.D. (2021). High-resolution mapping of the neutralizing and binding specificities of polyclonal sera post-HIV Env trimer vaccination. Elife 10, e64281. https://doi.org/10.7554/elife.64281.
- Jumper, J., Evans, R., Pritzel, A., Green, T., Figurnov, M., Ronneberger, O., Tunyasuvunakool, K., Bates, R., Žídek, A., Potapenko, A., et al. (2021). Highly accurate protein structure prediction with AlphaFold. Nature 596, 583–589. https://doi.org/10.1038/s41586-021-03819-2.
- Evans, R., O'Neill, M., Pritzel, A., Antropova, N., Senior, A., Green, T., Žídek, A., Bates, R., Blackwell, S., Yim, J., et al. (2022). Protein complex prediction with AlphaFold-Multimer. Preprint at bioRxiv. https://doi.org/ 10.1101/2021.10.04.463034.
- Clementel, D., Del Conte, A., Monzon, A.M., Camagni, G.F., Minervini, G., Piovesan, D., and Tosatto, S.C.E. (2022). RING 3.0: fast generation of probabilistic residue interaction networks from structural ensembles. Nucleic Acids Res. 50, W651–W656. https://doi.org/10.1093/nar/ gkac365.
- Song, G., He, W.T., Callaghan, S., Anzanello, F., Huang, D., Ricketts, J., Torres, J.L., Beutler, N., Peng, L., Vargas, S., et al. (2021). Cross-reactive serum and memory B-cell responses to spike protein in SARS-CoV-2 and endemic coronavirus infection. Nat. Commun. 12, 2938. https://doi.org/ 10.1038/s41467-021-23074-3.
- Calarese, D.A., Scanlan, C.N., Zwick, M.B., Deechongkit, S., Mimura, Y., Kunert, R., Zhu, P., Wormald, M.R., Stanfield, R.L., Roux, K.H., et al. (2003). Antibody Domain Exchange Is an Immunological Solution to Carbohydrate Cluster Recognition. Science 300, 2065–2071. https://doi. org/10.1126/science.1083182.
- Keeler, S.P., and Fox, J.M. (2021). Requirement of Fc-Fc Gamma Receptor Interaction for Antibody-Based Protection against Emerging Virus Infections. Viruses 13, 1037. https://doi.org/10.3390/v13061037.
- Burton, D.R. (2023). Antiviral neutralizing antibodies: from in vitro to in vivo activity. Nat. Rev. Immunol. 23, 720–734. https://doi.org/10.1038/s41577-023-00858-w.
- Alter, G., and Barouch, D. (2018). Immune Correlate-Guided HIV Vaccine Design. Cell Host Microbe 24, 25–33. https://doi.org/10.1016/j.chom. 2018 06 012
- Pittala, S., Bagley, K., Schwartz, J.A., Brown, E.P., Weiner, J.A., Prado, I.J., Zhang, W., Xu, R., Ota-Setlik, A., Pal, R., et al. (2019). Antibody Fab-Fc properties outperform titer in predictive models of SIV vaccine-induced protection. Mol. Syst. Biol. 15, e8747. https://doi.org/10.15252/msb.20188747.
- Chung, A.W., Ghebremichael, M., Robinson, H., Brown, E., Choi, I., Lane, S., Dugast, A.-S., Schoen, M.K., Rolland, M., Suscovich, T.J., et al. (2014). Polyfunctional Fc-effector profiles mediated by IgG subclass selection distinguish RV144 and VAX003 vaccines. Sci. Transl. Med. 6, 228ra38. https://doi.org/10.1126/scitranslmed.3007736.
- Haynes, B.F., Gilbert, P.B., McElrath, M.J., Zolla-Pazner, S., Tomaras, G.D., Alam, S.M., Evans, D.T., Montefiori, D.C., Karnasuta, C., Sutthent, R., et al. (2012). Immune-correlates analysis of an HIV-1 vaccine efficacy trial. N. Engl. J. Med. 366, 1275–1286. https://doi.org/10.1056/nejmoa1113425.
- Chung, A.W., Kumar, M.P., Arnold, K.B., Yu, W.H., Schoen, M.K., Dunphy, L.J., Suscovich, T.J., Frahm, N., Linde, C., Mahan, A.E., et al. (2015). Dissecting Polyclonal Vaccine-Induced Humoral Immunity against HIV Using Systems Serology. Cell 163, 988–998. https://doi.org/10.1016/j.cell.2015. 10.027.
- Richardson, S.I., Chung, A.W., Natarajan, H., Mabvakure, B., Mkhize, N.N., Garrett, N., Abdool Karim, S., Moore, P.L., Ackerman, M.E., Alter, G., and Morris, L. (2018). HIV-specific Fc effector function early in infection predicts the development of broadly neutralizing antibodies. PLoS Pathog. 14, e1006987. https://doi.org/10.1371/journal.ppat.1006987.



- Ackerman, M.E., Mikhailova, A., Brown, E.P., Dowell, K.G., Walker, B.D., Bailey-Kellogg, C., Suscovich, T.J., and Alter, G. (2016). Polyfunctional HIV-Specific Antibody Responses Are Associated with Spontaneous HIV Control. PLoS Pathog. 12, e1005315. https://doi.org/10.1371/journal. ppat.1005315.
- Alter, G., Dowell, K.G., Brown, E.P., Suscovich, T.J., Mikhailova, A., Mahan, A.E., Walker, B.D., Nimmerjahn, F., Bailey-Kellogg, C., and Ackerman, M.E. (2018). High-resolution definition of humoral immune response correlates of effective immunity against HIV. Mol. Syst. Biol. *14*, e7881. https://doi.org/10.15252/msb.20177881.
- Horwitz, J.A., Bar-On, Y., Lu, C.-L., Fera, D., Lockhart, A.A.K., Lorenzi, J.C.C., Nogueira, L., Golijanin, J., Scheid, J.F., Seaman, M.S., et al. (2017). Non-neutralizing Antibodies Alter the Course of HIV-1 Infection In Vivo. Cell 170, 637–648. https://doi.org/10.1016/j.cell.2017.06.048.
- 64. Dugast, A.-S., Chan, Y., Hoffner, M., Licht, A., Nkolola, J., Li, H., Streeck, H., Suscovich, T.J., Ghebremichael, M., Ackerman, M.E., et al. (2014). Lack of protection following passive transfer of polyclonal highly functional low-dose non-neutralizing antibodies. PLoS One 9, e97229. https://doi.org/10.1371/journal.pone.0097229.
- Burton, D.R., Hessell, A.J., Keele, B.F., Klasse, P.-J., Ketas, T.A., Moldt, B., Dunlop, D.C., Poignard, P., Doyle, L.A., Cavacini, L., et al. (2011). Limited or no protection by weakly or nonneutralizing antibodies against vaginal SHIV challenge of macaques compared with a strongly neutralizing antibody. Proc. Natl. Acad. Sci. USA 108, 11181–11186. https:// doi.org/10.1073/pnas.1103012108.
- Gray, G.E., Bekker, L.-G., Laher, F., Malahleha, M., Allen, M., Moodie, Z., Grunenberg, N., Huang, Y., Grove, D., Prigmore, B., et al. (2021). Vaccine Efficacy of ALVAC-HIV and Bivalent Subtype C gp120–MF59 in Adults. N. Engl. J. Med. 384, 1089–1100. https://doi.org/10.1056/ neimoa2031499
- 67. Anand, S.P., Grover, J.R., Tolbert, W.D., Prévost, J., Richard, J., Ding, S., Baril, S., Medjahed, H., Evans, D.T., Pazgier, M., et al. (2019). Antibody-Induced Internalization of HIV-1 Env Proteins Limits Surface Expression of the Closed Conformation of Env. J. Virol. 93, e00293-19. https://doi.org/10.1128/jvi.00293-19.
- Prévost, J., Richard, J., Medjahed, H., Alexander, A., Jones, J., Kappes, J.C., Ochsenbauer, C., and Finzi, A. (2018). Incomplete Downregulation of CD4 Expression Affects HIV-1 Env Conformation and Antibody-Dependent Cellular Cytotoxicity Responses. J. Virol. 92, e00484-18. https://doi.org/10.1128/jvi.00484-18.
- Richard, J., Veillette, M., Brassard, N., Iyer, S.S., Roger, M., Martin, L., Pazgier, M., Schön, A., Freire, E., Routy, J.-P., et al. (2015). CD4 mimetics sensitize HIV-1-infected cells to ADCC. Proc. Natl. Acad. Sci. USA 112, E2687–E2694. https://doi.org/10.1073/pnas.1506755112.
- Lee, W.S., Prévost, J., Richard, J., van der Sluis, R.M., Lewin, S.R., Pazgier, M., Finzi, A., Parsons, M.S., and Kent, S.J. (2019). CD4- and Time-Dependent Susceptibility of HIV-1-Infected Cells to Antibody-Dependent Cellular Cytotoxicity. J. Virol. 93, 1275. https://doi.org/10.1128/jvi.01901-18.
- Alsahafi, N., Ding, S., Richard, J., Markle, T., Brassard, N., Walker, B., Lewis, G.K., Kaufmann, D.E., Brockman, M.A., and Finzi, A. (2015). Nef Proteins from HIV-1 Elite Controllers Are Inefficient at Preventing Antibody-Dependent Cellular Cytotoxicity. J. Virol. 90, 2993–3002. https://doi.org/10.1128/jvi.02973-15.
- Rougé, L., Chiang, N., Steffek, M., Kugel, C., Croll, T.I., Tam, C., Estevez, A., Arthur, C.P., Koth, C.M., Ciferri, C., et al. (2020). Structure of CD20 in complex with the therapeutic monoclonal antibody rituximab. Science 367. 1224–1230. https://doi.org/10.1126/science.aaz9356.
- Oostindie, S.C., van der Horst, H.J., Lindorfer, M.A., Cook, E.M., Tupitza, J.C., Zent, C.S., Burack, R., VanDerMeid, K.R., Strumane, K., Chamuleau, M.E.D., et al. (2019). CD20 and CD37 antibodies synergize to activate complement by Fc-mediated clustering. Haematologica 104, 1841– 1852. https://doi.org/10.3324/haematol.2018.207266.

- van Osch, T.L.J., Nouta, J., Derksen, N.I.L., van Mierlo, G., van der Schoot, C.E., Wuhrer, M., Rispens, T., and Vidarsson, G. (2021). Fc Galactosylation Promotes Hexamerization of Human IgG1, Leading to Enhanced Classical Complement Activation. J. Immunol. 207, 1545–1554. https://doi.org/10. 4049/jimmunol.2100399.
- Hessell, A.J., Rakasz, E.G., Poignard, P., Hangartner, L., Landucci, G., Forthal, D.N., Koff, W.C., Watkins, D.I., and Burton, D.R. (2009). Broadly Neutralizing Human Anti-HIV Antibody 2G12 Is Effective in Protection against Mucosal SHIV Challenge Even at Low Serum Neutralizing Titers. PLoS Pathog. 5, e1000433. https://doi.org/10.1371/journal.ppat. 1000433
- Stadler, E., Burgess, M.T., Schlub, T.E., Khan, S.R., Chai, K.L., McQuilten, Z.K., Wood, E.M., Polizzotto, M.N., Kent, S.J., Cromer, D., et al. (2023). Monoclonal antibody levels and protection from COVID-19. Nat. Commun. 14, 4545. https://doi.org/10.1038/s41467-023-40204-1.
- Shingai, M., Donau, O.K., Plishka, R.J., Buckler-White, A., Mascola, J.R., Nabel, G.J., Nason, M.C., Montefiori, D., Moldt, B., Poignard, P., et al. (2014). Passive transfer of modest titers of potent and broadly neutralizing anti-HIV monoclonal antibodies block SHIV infection in macaques. J. Exp. Med. 211, 2061–2074. https://doi.org/10.1084/jem.20132494.
- Corey, L., Gilbert, P.B., Juraska, M., Montefiori, D.C., Morris, L., Karuna, S.T., Edupuganti, S., Mgodi, N.M., deCamp, A.C., Rudnicki, E., et al. (2021). Two Randomized Trials of Neutralizing Antibodies to Prevent HIV-1 Acquisition. N. Engl. J. Med. 384, 1003–1014. https://doi.org/10. 1056/nejmoa2031738.
- Moldt, B., Rakasz, E.G., Schultz, N., Chan-Hui, P.-Y., Swiderek, K., Weisgrau, K.L., Piaskowski, S.M., Bergman, Z., Watkins, D.I., Poignard, P., and Burton, D.R. (2012). Highly potent HIV-specific antibody neutralization in vitro translates into effective protection against mucosal SHIV challenge in vivo. Proc. Natl. Acad. Sci. USA 109, 18921–18925. https://doi.org/10.1073/pnas.1214785109.
- Parren, P.W., Marx, P.A., Hessell, A.J., Luckay, A., Harouse, J., Cheng-Mayer, C., Moore, J.P., and Burton, D.R. (2001). Antibody protects macaques against vaginal challenge with a pathogenic R5 simian/human immunodeficiency virus at serum levels giving complete neutralization in vitro. J. Virol. 75, 8340–8347. https://doi.org/10.1128/jvi.75.17.8340-8347.2001.
- Pauthner, M.G., Nkolola, J.P., Havenar-Daughton, C., Murrell, B., Reiss, S.M., Bastidas, R., Prévost, J., Nedellec, R., von Bredow, B., Abbink, P., et al. (2019). Vaccine-Induced Protection from Homologous Tier 2 SHIV Challenge in Nonhuman Primates Depends on Serum-Neutralizing Antibody Titers. Immunity 50, 241–252. https://doi.org/10.1016/j.immuni. 2018.11.011.
- Voss, N.R., Yoshioka, C.K., Radermacher, M., Potter, C.S., and Carragher, B. (2009). DoG Picker and TiltPicker: software tools to facilitate particle selection in single particle electron microscopy. J. Struct. Biol. 166, 205–213. https://doi.org/10.1016/j.jsb.2009.01.004.
- Zivanov, J., Nakane, T., Forsberg, B.O., Kimanius, D., Hagen, W.J., Lindahl, E., and Scheres, S.H. (2018). New tools for automated high-resolution cryo-EM structure determination in RELION-3. Elife 7, e42166. https://doi.org/10.7554/elife.42166.
- Niro, R.D., Mesin, L., Raki, M., Zheng, N.-Y., Lund-Johansen, F., Lundin, K.E.A., Charpilienne, A., Poncet, D., Wilson, P.C., and Sollid, L.M. (2010). Rapid generation of rotavirus-specific human monoclonal antibodies from small-intestinal mucosa. Am. Assoc. Immunol. 185, 5377–5383. https://doi.org/10.4049/jimmunol.1001587.
- Foote, J., and Winter, G. (1992). Antibody framework residues affecting the conformation of the hypervariable loops. J. Mol. Biol. 224, 487–499. https://doi.org/10.1016/0022-2836(92)91010-m.
- Abhinandan, K.R., and Martin, A.C.R. (2010). Analysis and prediction of VH/VL packing in antibodies. Protein Eng. Des. Sel. 23, 689–697. https://doi.org/10.1093/protein/gzq043.
- 87. Suloway, C., Pulokas, J., Fellmann, D., Cheng, A., Guerra, F., Quispe, J., Stagg, S., Potter, C.S., and Carragher, B. (2005). Automated molecular



microscopy: The new Leginon system. J. Struct. Biol. 151, 41–60. https://doi.org/10.1016/j.jsb.2005.03.010.

- Lander, G.C., Stagg, S.M., Voss, N.R., Cheng, A., Fellmann, D., Pulokas, J., Yoshioka, C., Irving, C., Mulder, A., Lau, P.-W., et al. (2009). Appion: An integrated, database-driven pipeline to facilitate EM image process-
- ing. J. Struct. Biol. *166*, 95–102. https://doi.org/10.1016/j.jsb.2009. 01.002.
- Pettersen, E.F., Goddard, T.D., Huang, C.C., Couch, G.S., Greenblatt, D.M., Meng, E.C., and Ferrin, T.E. (2004). UCSF Chimera–a visualization system for exploratory research and analysis. J. Comput. Chem. 25, 1605–1612. https://doi.org/10.1002/jcc.20084.





STAR***METHODS**

KEY RESOURCES TABLE

REAGENT or RESOURCE	SOURCE	IDENTIFIER
Antibodies		
anti-Hu IgG-APC	Jackson Laboratories	RRID: AB_2340526
Human IgG Isotype Control	ThermoFisher Scientific	RRID: AB_243591
anti-CD64	Caltag Medsystems	Cat#IQP-569P
anti-CD32b	ThermoFisher Scientific	RRID: AB_2608963
anti-CD16-APC	R&D Systems	Cat#FAB2546A
anti-Mouse IgG (H + L),Texas Red-X	ThermoFisher Scientific	RRID: AB_2556781
anti-Hu IgG-APC	Jackson Laboratories	RRID: AB_2340526
anti-Goat IgG	Jackson Laboratories	RRID: AB_2340407
Human IgG Isotype Control	ThermoFisher Scientific	RRID: AB_243591
anti-CD14-APC	BD Biosciences	RRID: AB_398596
anti-CD64	Caltag Medsystems	Cat#IQP-569P
anti-CD16-FITC	BD Biosciences	RRID: AB_395806: Cat#555406
anti-CD32b	ThermoFisher Scientific	RRID: AB_2608963
anti-CD16-APC	R&D Systems	RRID: AB_395806; Cat#FAB2546A
anti-CD56-PE	BD Biosciences	RRID: AB_395906
anti-Mouse IgG (H + L),Texas Red-X	ThermoFisher Scientific	RRID: AB_2556781
anti-Hu IgG F(ab') ₂ -Peroxidase	Jackson Laboratories	RRID: AB_2337585
anti-Goat IgG	Jackson Laboratories	RRID: AB_2340407
numan IgG Isotype Control	Invitrogen	31154
anti-CD14-APC	BD Biosciences	RRID: AB_398596
anti-CD64 antibody	Caltag Lab	RRID: AB_1480526
anti-CD16-FITC	BD Biosciences	RRID: AB395806; Cat#555406
anti-FCGR2B Polyclonal Antibody	Thermo Fisher Scientific	RRID: AB_2608963; PA5-47122
anti-CD56-PE	BD Biosciences	RRID: AB_395906
goat anti-Mouse IgG (H + L) Cross-Adsorbed Secondary Antibody, Texas Red	Invitrogen	RRID: AB_2556781; T-862
anti-Hu IgG F(ab')₂-Peroxidase	Jackson Laboratories	RRID: AB_2337585
Allophycocyanin (APC) AffiniPure TM F(ab')₂ Fragment Donkey Anti-Goat IgG (H + L)	Jackson Immuno	RRID: AB_2340407; 705-136-147
numan IgG Isotype Control	Invitrogen	31154
anti-CD64 antibody	Caltag Lab	RRID: AB_1480526; CD6400
anti-FCGR2B Polyclonal Antibody	Thermo Fisher Scientific	RRID: AB_2608963; PA5-47122
goat anti-Mouse IgG (H + L) Cross-Adsorbed Secondary Antibody, Texas Red	Invitrogen	T-862
Allophycocyanin (APC) AffiniPure TM F(ab')₂ Fragment Donkey Anti-Goat IgG (H + L)	Jackson Immuno	RRID: AB_2340407; 705-136-147
Biological samples		
Leukopak	STEMCELL	Cat#70500
Chemicals, peptides, and recombinant proteins		
ipofectamine 2000	ThermoFisher Scientific	Cat#11668027
Puromycin	Sigma-Aldrich	Cat#P9620
40K PEI	Polysciences	Cat#24765
NeutrAvidin	ThermoFisher Scientific	Cat#31000
Tween 20	ThermoFisher Scientific	Cat#BP337500

(Continued on next page)



Continued		
REAGENT or RESOURCE	SOURCE	IDENTIFIER
ГМВ	ThermoFisher Scientific	Cat#34028
Tween 20	ThermoFisher Scientific	Cat#BP337500
cysteine	ThermoFisher Scientific	Cat#44889
Alpha-iodoacetamide	Millipore	Cat#407710
Papain	Sigma-Aldrich	Cat#P3125
Alpha-iodoacetamide	Millipore	Cat#407710
Ammonium Chloride	STEMCELL	Cat#07850
Papain	Sigma-Aldrich	Cat#P3125
Ammonium Chloride	STEMCELL	Cat#07850
Cryopreservation medium	STEMCELL	Cat#07931
Critical commercial assays		
Jurkat CD16 NFAT Reporter Assay	Invivogen	Cat#jktl-nfat-cd16
Human NK Cell Isolation Kit	STEMCELL	Cat#17955
Human Monocyte without CD16 depletion solation Kit	STEMCELL	Cat#19058
DNAEasy Blood and Tissue Kit	QIAGEN	Cat#69504
Human Monocyte without CD16 depletion solation Kit	STEMCELL	Cat#19058
Deposited data		
EMD-42907, EMD-42908, EMD-42909, EMD-42910, EMD-42912, and EMD-42913	EMDB	https://www.ebi.ac.uk/emdb/
Experimental models: Cell lines		
HEK293T	ATCC	Cat#CRL-3216
Freestyle 293-F	ThermoFisher	Cat#R79007
Jurkat Lucia NFAT CD16	Invivogen	Cat#jktl-nfat-cd16
THP-1	ATCC	Cat#TIB-202
Oligonucleotides		
cf. supplementary Table	this study	Table S1
Recombinant DNA		
Lenti-HF1RA-P2A-GFP-PGK-Puro	Addgene	#110866
Display-BirA-ER	Addgene	#20856
Software and algorithms		
Prism 9 and 10	GraphPad	https://www.graphpad.com
AlphaFold2	DeepMind	https://deepmind.google/ technologies/alphafold/
PyMol 2.5.0	Warren DeLano	https://www.pymol.org
RING3.0	BioComputingUP	https://ring.biocomputingup.it
Appion/Leginon	https://github.com/ leginon-org/leginon	N/A
DoGpicker	Voss et al. ⁸²	https://emg.nysbc.org//projects/ software/wiki/DoGpicker
Relion 3.0	Zivanov et al. ⁸³	https://github.com/3dem/relion.git
Cinema 4D	Maxon Inc.	https://www.maxon.net/en/cinema- 4d?gad_source=1&gbraid=0AAAAApQN fLTcnKhPGScpNXlh7KsPVzCL&gclid= EAlalQobChMI_rWI7Ja-igMVJiVECB0B> AdvEAAYASAAEglk4fD_BwE
Other		
FITC Neutravidin FluoSpheres	ThermoFisher Scientific	Cat#F8776
Protein A Biosensors	Sartorius	Cat#18-5010





EXPERIMENTAL MODEL AND STUDY PARTICIPANT DETAILS

All human PBMCs used for this study originate from two healthy male individuals and were procured from STEMCELL. Due to the low number of individuals, no generalization regarding the impact of gender or race on the results presented in this study can be made. Human primary cell work was approved by WCG IRB (STEMCELL) and Scripps IRB (The Scripps Research Institute). Informed consent from all donors was obtained by STEMCELL technologies or their contractors prior to donation.

All cell lines used in this study were purchased from commercial vendors or repositories who guaranteed their authenticity and absence of mycoplasma contamination.

METHOD DETAILS

Expression constructs

In silico structure prediction and probabilistic network interaction analysis

Amino acids 31–663 of RT design candidates were subjected to structure prediction as a trimer using the AlphaFold2 multimer algorithm. Resulting predictions were structurally aligned and combined into a single multi-state file in PyMol 2.5.0 before they were subjected to probabilistic network analysis using the RING3.0 software package. Designs were visually scored for proper trimer folding and epitope surface exposure, and designs with high surface exposure and a low number of changing interactions between individual predictions were prioritized.

Membrane-bound env

For the generation of mbRT expression constructs, plasmid pLenti-HF1RA-P2A-GFP-PGK-Puro (Addgene #110866) was modified to contain an EcoRI site before the P2A cleavage site by QuickChange site-directed mutagenesis using forward primer 5′-GTCAAGCT AAGAAAAGAATTCAGGCAGCGCGCCACCAAC-3′ in conjunction with reverse primer 5′- GTTGGTGGCGCGCGCTGCCTGAATT CTTTTCTTAGCTTGAC-3′. The EcoRI x NotI fragment was then exchanged with a DNA string containing a T2A instead of a P2A cleavage site. The BG505-NFL.711 open reading frame (ORF) was modified to contain a 5′ BamHI site, as well as a Kozak sequon and an EcoRI site at its 3′ end. The reading frame was synthesized as two strings containing 30–40 nucleotide overlaps to facilitate Gibson assembly into the BamHI x EcoRI-digested modified pLenti vector. For the construction of individual mbRT constructs, mutations were introduced in one of two ways. In the cases of RT-V2t and RT-Bttm, the reading frame was similarly synthesized as three DNA strings, after which Gibson assembly was performed with the same digested vector. For the remaining constructs, two DNA fragments were generated via PCR using Phusion Hot Start II DNA Polymerase (Thermo #F-549L), the pLenti-BG505wt template, and the following primer scheme: the first fragment used forward primer 5′- GGTTTGCCGCCAGAACACAGG-3′ and the tag reverse primer, and the second fragment used the tag forward primer and reverse primer 5′- CTTCCTCTGCCCTCGCCG-3′. Gibson assembly was then performed with the same digested vector.

Soluble biotinylated env

For the construction of the sRTs, the extracellular domain of the respective construct was PCR-amplified using forward primer 5'-GA CACCGGGACCGATCCAGCCTCCGGAGAATTCGCCACCATGCCTATGGGATC-3' and reverse primer 5'-GGTGATGCTTAGTTCCGG CGGATCCCAGGGCCAGCAGGTCCTGCTCG-3' to truncate the ORF before the transmembrane region and to introduce Gibson overhangs compatible with an EcoRI x BamHI-digested modified pcDNA3.4 vector containing a C-terminal in-frame hexahistidine tag, a BirA recognition sequence, and a stop codon. Gibson assembly was then performed on the resulting DNA fragment and digested vector. **Antibodies**

All antibody V regions were synthesized as strings and cloned into pAbVec expression vectors⁸⁴ using Agel and Sall restriction sites for the IgG1 heavy chain (GenBank FJ475055.1), Agel and BsiWI for kappa chain constructs (GenBank FJ475056.1), and Agel and Xhol for lambda chain constructs (GenBank FJ517647).

The mouse heavy and light chain V region sequences of mAb 12CA5 (GenBank LC522514 and LC522515) were humanized via complementarity-determining region (CDR) grafting. To this end, the most closely related human V regions for both the mouse heavy and light chains were identified using IMGT's V-Quest algorithm (https://www.imgt.org/IMGT_vquest/input). Mouse CDRs were then grafted onto their corresponding locations of the respective human IGHV3-21*03 and IGKV4-1*01 V regions. To optimize CDR orientation, additional human framework amino acids⁸⁵ were substituted for their mouse counterparts (N40S for CDRH1, and S54A/S55T/A68P for CDRH2; A40T for CDRL1; IMGT numbering). Last, we used the VH/VL packaging angle prediction⁸⁶ to generate one version in which the packaging angle of the humanized 12CA5 was altered to match the –47.9° torsion angle of the mouse antibody by adding a G47D mutation to the heavy chain. Sequences were modified for in-frame cloning into the appropriate pAbVec vectors, as outlined above, and synthesized as DNA strings (Geneart). Functionality of humanized 12CA5 versions was confirmed by ELISA, and the unoptimized version, as well as an Fc null variant thereof (12CA5-LALAPG), was chosen for all experiments.

Generation of stable HEK293T cell lines

One day prior to transfection, 1.5 million HEK293T cells (293T, ATCC CRL-3216) were seeded in a 10cm culture dish with 10mL of 293T transfection medium consisting of DMEM (Corning 15013CV) supplemented with 10% fetal bovine serum (FBS) and 2mM L-glutamine (Corning 25005Cl). 293Ts were transfected with 24µg of respective mbRT DNA using 42µL of Lipofectamine 2000 (Invitrogen 11668027). After 1 day of culture, medium was replaced with 10mL of 293T culture medium consisting of DMEM



supplemented with 10% FBS, 2mM L-glutamine, and 100 IU/mL-100 μg/mL Penicillin-Streptomycin (Corning 30002CI). After another day of culture, cells were rinsed with PBS, incubated with trypsin (Corning 25053CI) for 3 min, and transferred to a new 10cm culture dish in 10mL of 293T selection medium consisting of DMEM supplemented with 10% FBS, 2mM L-glutamine, 100IU/mL-100μg/mL Penicillin-Streptomycin, and 10μg/mL Puromycin (Sigma P9620). After one week of culture under selection, the first round of subcloning was performed by either plucking or limiting dilution. For plucking, a fluorescent microscope was sterilized and brought into a biosafety cabinet; the cell culture dish was visualized with the GFP channel; and GFP-positive cell colonies were scraped and captured with a P20 pipette. Colonies were seeded in wells of a tissue culture-treated 96 well plate (Corning 3595) with 293T selection medium and expanded as necessary. For limiting dilution, cells were trypsinized and resuspended to a density of 2000 cells/mL in 293T selection medium. 200μL of cell suspension were added to the top left well of a tissue culture-treated 96 well plate and serially diluted 1/2 down the row, which was then serially diluted 1/2 down the plate, all in 293T selection medium. After two weeks of culture, monoclonal GFP-positive colonies were selected for expansion. Once subclones were sufficiently expanded, cells were screened via flow cytometry (BD FACSLyric) for GFP expression and 12CA5 binding. Double-positive subclones were selected for further expansion. A second round of subcloning was performed on the best first-round subclones via fluorescence-activated cell sorting (FACS, BD FACSMelody), gating on the top 1% of double-positive cells.

sRT production

1L of Freestyle 293-F cells (Gibco R79007) at a density of 1 million cells/mL in Freestyle Expression Medium (Gibco 12338018) was co-transfected with 350μg of the respective sRT plasmid, 150μg of Furin, and 190μg of pDisplay-BirA-ER (Addgene #20856) using 2mL of 40K PEI (Polysciences 49553937). After 6 days of culture, the solution was harvested and centrifuged for 20 min at 2000xg at 4°C. Supernatant was clarified with a 0.22μm filter, and 1mL of 1% sodium azide was added. Clarified supernatant was then passed over a Nickel column (Thermo 88222) and washed with two wash buffers containing 40mM and 60mM imidazole, respectively. sRT protein was eluted with elution buffer containing 250mM of imidazole. Eluted proteins were buffer exchanged into TBS via several rounds of centrifugation for 10 min at 2000xg at 4°C in a 100kDa MWCO Amicon tube (MilliporeSigma UFC905008), then purified and fractionated on AKTA Pure using a Superose 6 increase 10/300 GL column (Cytiva 29091596). Fractions were collected, concentrated to 1 mg/mL via several rounds of centrifugation for 5 min at 2000xg at 4°C using a 30kDa MWCO Amicon tube (MilliporeSigma UFC803024), aliquoted, and stored at −80°C.

Cell binding assay

Antibodies were diluted to 40 μg/mL in FACS Buffer consisting of PBS supplemented with 2% FBS. Antibodies were then serially diluted 1/4 7 times in duplicate with FACS Buffer, and 50μL of antibody dilutions were transferred to 96 well plates (Corning 3788). mbRT target cells were rinsed with PBS, trypsinized, and collected in 293T selection medium. Cells were centrifuged for 5 min at 150xg and resuspended at a density of 2 million cells/mL in FACS Buffer. 50μL of target cell suspension were transferred to antibody dilutions and incubated for 1 h at RT. After incubation, cells were washed 3 times with FACS Buffer via repeated centrifugation for 3 min at 500xg and resuspension in FACS Buffer. 50μL of anti-Hu IgG Allophycocyanin (APC) AffiniPure F(ab')₂ Fragment Donkey Anti-Human IgG (H + L), (Jackson 709-136-149) diluted 1/5000 in FACS buffer were then added, and cells were incubated for 20 min at 4°C in the dark. After incubation, cells were washed 3 times with FACS Buffer. 50μL of Cytofix/Cytoperm (BD 554722) were then added, and cells were incubated for 20 min at 4°C in the dark. After incubation, cells were washed 2 times with FACS Buffer. GFP and APC fluorescence were measured via flow cytometry (BD FACSLyric) gated on live cells with acquisition limits of 5000 events or 60 s. Averaged GFP MFI was determined by averaging the geometric mean fluorescence intensity of GFP-positive cells across 192 samples. Both half-maximal effective concentration and maximal binding were interpolated using a Hill-curve-based non-linear curve fitting model (GraphPad Prism 9 + 10). Normalized maximal binding was calculated by dividing the RLU signal by the ratio of the averaged GFP MFI of the respective mbRT cell line to the pan assay mean GFP MFI.

FcYR FACS

Monocytes or THP-1 cells were collected by centrifugation for 5 min at 350xg and resuspended at a density of 1 million cells/mL in FACS Buffer. 200μ L of each cell suspension were transferred to 5mL FACS tube (Corning ref. 352235) and incubated with $20\,\mu$ g/mL of human lgG (Invitrogen ref. 31154) for 30 min to block $Fc\gamma R$ binding. For the staining, 10μ L of anti-CD64 antibody (Ref. Caltag Lab CD6400), 15μ L of anti-CD32b (Thermo Fisher Ref. PA5-47122), 10μ L of anti-CD32a/b and 20μ L of Allophycocyanin (APC) anti-FcGRIIIa/b (R&D Systems Ref. FAB2546A) were used per tube. All stains were incubated at $4^{\circ}C$ in the dark for 1 h. After incubation, cells were washed 3 times with FACS Buffer and incubated with secondary antibodies (15μ L of Texas Red anti-mouse lgG (H + L) (Invitrogen Ref. T-862) and 15μ L of Allophycocyanin (APC) anti-Goat lgG (Jackson Immuno. Ref. 705-136-147)) at $4^{\circ}C$ in the dark for 1 h. After incubation, cells were washed 3 times with FACS Buffer and read on a ZE5 FACS scanner (BioRad).

FcyRIIIa signaling assays

Antibodies were diluted to $40 \,\mu\text{g/mL}$ in signaling assay medium consisting of IMDM (Gibco 12440053) supplemented with 10% FBS, 2mM L-glutamine, and $100 \,\text{IU/mL-}100 \,\mu\text{g/mL}$ Penicillin-Streptomycin and centrifuged for 15 min at 20,000xg at 4°C in $0.22\mu\text{m}$ filter tubes (Costar UX0193730). Antibodies were then diluted 1/10 in duplicate with signaling assay medium, and $50\mu\text{L}$ of antibody dilutions were transferred to tissue culture-treated 96 well plates (Corning 3595). In parallel, mbRT target cells were rinsed with PBS,





trypsinized, and collected in 293T selection medium. Cells were centrifuged for 5 min at 150xg and resuspended at a density of 2 million cells/mL in signaling assay medium. 50μ L of target cell suspensions were transferred to antibody dilutions and incubated for 3 h at $37^{\circ}\text{C}/5\%\text{CO}_2$. Meanwhile, Jurkat-Lucia NFAT-CD16 (Invivogen jktl-nfat-cd16) effector cells were collected, centrifuged for 5 min at 125xg, resuspended in PBS, centrifuged again, and resuspended at a density of 2 million cells/mL in signaling assay medium. 100μ L of effector cell suspension were transferred to target cells and co-cultured overnight at $37^{\circ}\text{C}/5\%\text{CO}_2$. Prior to preparing samples, Quanti-Luc Gold substrate (Invivogen rep-qlcg5) was prepared as per the manufacturer's instructions. 50μ L of supernatant were then transferred to white half-well 96 well plates (Corning 3688). 45μ L of substrate were injected to samples, and luminescence was immediately measured. Normalized relative light units (RLUs) were calculated by dividing the raw RLU signal by the ratio of the averaged GFP MFI of the respective mbRT cell line to the pan assay mean GFP MFI.

ADCP assay

10μL of 1μm FITC-labeled FluoSpheres NeutrAvidin Microspheres (Invitrogen #F8776) per sRT well plate were washed 3 times with 1mL of PBS via centrifugation for 10 min at 5,000xg and resuspension in PBS. Beads were finally resuspended in 300μL of PBS. sRTs were then added to a concentration of 30 µg/mL, and solutions were gently agitated for 2 h at 4°C in the dark. sRT-coated beads were washed 3 times with PBS and resuspended in THP-1 (ATCC TIB-202) culture medium consisting of RPMI1640 (Corning 10040CV) supplemented with 10% FBS, 2mM L-glutamine, and 100 IU/mL-100 μg/mL Penicillin-Streptomycin. Antibodies were centrifuged for 15 min at 20,000xg at 4°C. Then, antibodies were serially diluted 3-fold 11 times in singlet or duplicate with a starting concentration of 30 μg/mL in THP-1 culture medium, and 20μL of antibody dilutions were transferred to tissue culture-treated 96 well plates (Corning 3799). 10µL of sRT-coupled beads were added to antibody dilutions and incubated for 2 h at 37°C/5%CO₂. Meanwhile, THP-1 cells or monocytes were collected, centrifuged for 5 min at 500xg, resuspended in THP-1 culture medium, centrifuged again, and resuspended at a density of 500,000 cells/mL in THP-1 culture medium. 95μL of THP-1 or monocyte cell suspension were transferred to opsonized sRT-coated beads and cultured overnight (THP-1 cells) or for 4 h (monocytes) at 37°C/5%CO2. After incubation, cells were washed 3 times with FACS Buffer via centrifugation for 5 min at 500xg and resuspension in FACS Buffer. 50μL of Cytofix/ Cytoperm were then added, and cells were incubated for 15 min at 4°C in the dark. After incubation, cells were washed 2 times with FACS Buffer. GFP fluorescence was measured via flow cytometry (BD FACSLyric) gated on CD14 positive live cells with acquisition limits of 5000 events or 60 s. The phagocytic score was calculated as the GFP MFI of GFP-positive cells multiplied by the percentage of GFP-positive cells The phagocytic score was then adjusted by subtracting the averaged phagocytic score of a given sRT with no antibody. Both half-maximal phagocytic concentration and maximal phagocytic score were interpolated using a Hill-curvebased non-linear curve fitting model (GraphPad Prism 9 + 10).

NK cell isolation

For the isolation of NK cells from frozen peripheral blood mononuclear cells (PBMCs), 400 million PBMCs were thawed and cultured in PBMC culture medium consisting of RPMI1640 supplemented with 10% FBS, 2mM L-glutamine, and 100 IU/mL-100 μg/mL Penicillin-Streptomycin overnight at 37°C/5%CO₂. PBMCs were collected, centrifuged for 10 min at 300xg, and resuspended at a density of 50 million cells/mL in PBMC culture medium. NK cells were then isolated using the STEMCELL EasySep Human NK Cell Isolation Kit (STEMCELL 17955) according to the manufacturer's instructions. In brief, 50μL of Isolation Cocktail (STEMCELL 17955C) per mL of PBMC solution were added and incubated for 10 min. Magnetic beads (STEMCELL 50103) were then thoroughly vortexed, and 50μL per mL of PBMC solution were added. Solution volume was adjusted with PBMC culture medium, and solution was incubated for 10 min in magnet (STEMCELL 180002). Solution was carefully collected and incubated again for 5 min in magnet. NK cell purity (typically between 70% and 90%) was determined by flow cytometry using anti-CD14 (BD #555399), CD16 (BD#555406), and CD56 (BD# 561903) antibodies.

Monocyte isolation

For the isolation of monocytes from PBMCs, 50–100 million PBMCs were thawed quickly in a 37° C water bath and washed in RPMI1640 supplemented with 10% FBS, 2mM L-glutamine, and 100 IU/mL-100 $\mu\text{g/mL}$ Penicillin-Streptomycin to remove any residual DMSO. PBMCs were collected, centrifuged for 10 min at 300xg, and resuspended at a density of 50 million cells/mL in PBS with 2% FBS. Monocytes were then isolated using the EasySep Human Monocyte Enrichment Kit without CD16 Depletion (STEMCELL 19058) according to the manufacturer's instructions. In brief, $50\mu\text{L}$ of Isolation Cocktail (STEMCELL 19058C.2) per mL of PBMC solution were added and incubated for 10 min at 4° C. Magnetic beads (STEMCELL 19550) were then thoroughly vortexed, and $50\mu\text{L}$ per mL of PBMC solution were added and incubated for 5 min at 4° C. Solution volume was adjusted with PBS with 2% FBS, and solution was incubated for 3 min in magnet (STEMCELL 180001). Solution was carefully collected in new tube for use in the ADCP assay.

ADCC assay

Antibodies were diluted to 40 μ g/mL in PBMC culture medium consisting of RPMI1640 supplemented with 10% FBS, 2mM L-glutamine, and 100 IU/mL-100 μ g/mL Penicillin-Streptomycin and centrifuged for 15 min at 20,000xg at 4°C in 0.22 μ m filter tubes (Costar UX0193730). Antibodies were then diluted 1/10 in duplicate with PBMC culture medium, and 50 μ L of antibody dilutions were transferred to tissue culture-treated 96 well plates (Corning 3595). In parallel, mbRT target cells were rinsed with PBS, trypsinized, and collected in 293T selection medium. mbRT target cells were mixed with plain 293Ts to a ratio of 1:4 mRTs to 293Ts. Cells were



centrifuged for 5 min at 150xg and resuspended at a density of 1 million cells/mL in PBMC culture medium. 50 μ L of target cell suspension were transferred to antibody dilutions and incubated for 3 h at 37°C/5%CO $_2$. Meanwhile, NK cells were isolated from PBMCs cultured overnight (see NK cell isolation), and NK cells were brought to a density of 500,000 cells/mL. 100 μ L of NK cell suspension were transferred to target cells and co-cultured overnight at 37°C/5%CO $_2$. After co-culture, cells were rinsed with PBS, 50 μ L of trypsin were added, and cells were incubated for 8 min at 37°C/5%CO $_2$. 150 μ L of FACS Buffer were added, and cells were thoroughly mixed and transferred to non-tissue culture-treated 96 well plates (Corning 3788). Cells were washed with FACS Buffer via centrifugation for 3 min at 500xg and resuspension in FACS Buffer. 50 μ L of Cytofix/Cytoperm were then added, and cells were incubated for 20 min at 4°C. After incubation, cells were washed 2 times with FACS Buffer. GFP fluorescence was measured via flow cytometry (BD FACSLyric) gated on live cells with acquisition limits of 5000 events or 60 s. Percent specific killing was calculated as (100% · [1-(%GFP+ w/o mAb - %GFP+ w/mAb)/%GFP+ w/o mAb], where %GFP+ w/o mAb is the percent of GFP-positive target cells with no antibody for a given target cell line and %GFP+ w/mAb is the percent of GFP-positive target cells with a given antibody for a given target cell line. As with the Fc γ RIIIa signaling assays, normalized killing was calculated by dividing the percent killing by the ratio of the averaged GFP MFI of the respective mbRTto the pan assay mean GFP MFI.

Binding ELISA

Biolayer interferometry

Antigen solutions were prepared for each sRT by adding 222nmol of sRT protein to 250μ L of baseline buffer consisting of PBS with 0.05% Tween 20 (v/v) and gently mixing. A 25 μ g/mL solution of 12CA5 mAb was prepared in baseline buffer. Octet ProA Biosensors (Sartorius 10–5010) were pre-hydrated with baseline buffer for 20 min at RT. Baseline buffer, antigen solutions, and antibody solution were added to a black 96 well plate (Greiner Bio-One cat. 655209). Assay was run using Octet BLI Discovery 12.2.2.20 software and the OCTET HTX by loading sensors with the antibody solution, associating with the antigen solutions, and dissociating in baseline buffer. K_D , k_{DD} , and k_{DD} were quantified on the Octet Analysis Studio 12.2.2.26 software.

Fab digestion

Prior to Fab digestion, digestion buffer (DB) was prepared as 10mM EDTA in PBS, pH 10.0. The day of digestion, digestion buffer with cysteine (DBC) was prepared by dissolving L-cysteine (Pierce 44889) in DB to a concentration of 3.5 mg/mL, and 10x stop solution was prepared by dissolving iodoacetamide (Millipore 407710) in DB to a concentration of 55.5 mg/mL. 20μ L of papain buffered aqueous suspension (Millipore P3125) were diluted in 480 μ L of sterile water. Papain and IgG at a mass ratio of 1:74 were diluted in DBC such that the volume of DBC was >70% total reaction volume and incubated for 2.5 h at 37°C. 10x stop solution was added, and Fabs were dialyzed into TBS with a 10kDa MWCO dialysis cassette (Thermo 66380).

Complex formation

 $50\mu g$ of sRT and 10-fold molar excess of Fab were transferred to a 10kDa MWCO spin tube (Millipore UFC5010), concentrated to $70\mu L$ via several rounds of centrifugation for 5 min at 2000xg, and incubated overnight at 4° C. Complexes were purified and fractionated on AKTA Pure using a Superose 6 increase 10/300 GL column.

Negative-stain electron microscopy

sRT-Fab complexes were diluted to 30 μg/mL, adsorbed onto glow-discharged copper mesh grids, and stained with 2% (w/v) uranyl formate for 60 s. Automated data collection was set up using Leginon⁸⁷ on either a 120 keV FEI Tecnai Spirit equipped with an FEI Eagle 4K CCD (52,000× magnification; 2.06 Å pixel size), a 120 keV FEI TF20 equipped with a TVIPS TemCam F416 CMOS (62,000× magnification; 1.68 Å pixel size), or a Thermo Fisher Scientific Talos equipped with Thermo Fisher Scientific CETA 4K CMOS (73,000× magnification; 1.98 Å pixel size). Micrographs were saved in the Appion database.⁸⁸ Particles were picked using DoGpicker⁸² and processed in Relion 3.0.⁸³ Maps were visualized using UCSF Chimera.⁸⁹

Glycoanalysis

Three aliquots of each sRT were denatured for 1h in 50 mM Tris/HCl, pH 8.0 containing 6M urea and 5mM dithiothreitol (DTT). Next, sRTs were reduced and alkylated by adding 20 mM iodoacetamide (IAA) and incubating for 1 h in the dark, followed by a 1-h





incubation with 20 mM DTT to eliminate residual IAA. Alkylated sRTs were buffer exchanged into 50 mM Tris/HCl, pH 8.0 using 10kDa MWCO spin columns (Cytiva 28932225) and separately digested overnight using trypsin (Promega VA900A), chymotrypsin (Promega V1062), or alpha lytic protease at a ratio of 1:15 (w/w). Peptides were dried and extracted using an Oasis HLB 96 well plate (Waters WAT058951). Peptides were then dried again, resuspended in 0.1% formic acid, and analyzed by nanoLC-ESI MS with an Ultimate 3000 HPLC (Thermo IQLAAAGABHFAPBMBFC) system coupled to an Orbitrap Eclipse mass spectrometer (Thermo) using stepped higher energy collision-induced dissociation (HCD) fragmentation. Peptides were separated using an EasySpray PepMap RSLC C18 column (75 μ m × 75 cm). A trapping column (PepMap 100 C18 3 μ M 75 μ M × 2 cm) was used in line with the LC prior to separation with the analytical column. The LC conditions were as follows: 280-min linear gradient consisting of 5–40% acetonitrile in 0.1% formic acid over 255 min followed by 20 min of alternating 95% acetonitrile in 0.1% formic acid and 2.5% acetonitrile in 0.1% formic acid, used to ensure all the sample had eluted from the column. The flow rate was set to 300 nL/min. The spray voltage was set to 2.5 kV and the temperature of the heated capillary was set to 55°C. The ion transfer tube temperature was set to 275°C. The scan range was 375–1500 m/z. Stepped HCD collision energy was set to 15, 25 and 45%, and the MS2 for each energy was combined. Precursor and fragment detection were performed using an Orbitrap at a resolution of MS1 = 120,000, MS2 = 30,000. The AGC target for MS1 standard and injection times were set to auto, which involves the system setting the two parameters to maximize sensitivity while maintaining cycle time.

Glycopeptide fragmentation data were extracted from the raw file using Byos (Version 4.6 Protein Metrics Inc.). The glycopeptide fragmentation data were evaluated manually for each glycopeptide: the peptide was scored as true-positive when the correct b and y fragment ions were observed along with oxonium ions corresponding to the glycan identified. The MS data was searched using the Protein Metrics 305 N-glycan library with sulfated glycans added manually. The relative amounts of each glycan at each site as well as the unoccupied proportion were determined by comparing the extracted chromatographic areas for different glycotypes with an identical peptide sequence. All charge states for a single glycopeptide were summed. The precursor mass tolerance was set at 4 ppm and 10 ppm for fragments. A 1% false discovery rate (FDR) was applied. The relative amounts of each glycan at each site as well as the unoccupied proportion were determined by comparing the extracted ion chromatographic areas for different glycopeptides with an identical peptide sequence. Glycans were categorized according to the composition detected.

PBMC isolation

Fresh human peripheral blood acquired via apheresis (STEMCELL 70500) was received and immediately processed. Blood was collected and centrifuged for 8 min at 336xg, and serum was carefully removed. Cell pellets were resuspended in ammonium chloride (STEMCELL 07850) and incubated for 10 minutes on ice. Cell suspensions were topped off with PBS and centrifuged for 8 min at 336xg. Cell suspensions were then washed 2 times with PBMC culture medium consisting of RPMI1640 supplemented with 10% FBS, 2mM L-glutamine, and 100 IU/mL-100 μ g/mL Penicillin-Streptomycin via repeated centrifugation for 8 min at 336xg and resuspension in PBMC culture medium. Isolated PBMCs were either used immediately or frozen in 400 million cell aliquots using CryoStorCS10 cryopreservation medium (STEMCELL 07931). For the determination of the donor's genotype, Fc γ R-relevant exons of the Fc γ RIIa and IIIa gene were amplified from genomic DNA extracted according to the manufacturer's instructions (Qiagen DNEasy 69504), the PCR product subcloned, and 5–10 clones sequenced. Primers of amplification were 5′-GGAAAATCCCAGAAA TTCTCCC-3′ x 5′-CAACAGCCTGACTACCTATTACCTGG-3′ (Fc γ RIIa), and 5′- CCTTCACAATTTCTGCAGCCACT-3′ x 5′-CCCAG TGTGATTGCAGGTTCCA-3′ (Fc γ RIIIa).

QUANTIFICATION AND STATISTICAL ANALYSES

All statistical analyses were performed in GraphPad 9 or 10. Tests employed, dispersion and precision measures as well as significance levels are listed in the corresponding figure legend.